STARS

Electronic Theses and Dissertations, 2020-

2022

Development of Holographic Phase Masks for Wavefront Shaping

Nafiseh Mohammadian

University of Central Florida

Showcase of Text, Archives, Research & Scholarship

DEVELOPMENT OF HOLOGRAPHIC PHASE MASKS FOR WAVEFRONT SHAPING

by

NAFISEH MOHAMMADIAN

B.S. University of Isfahan, 2008
M.S. University of Central Florida, 2018

A dissertation submitted in partial fulfillment of the requirements
for the degree of Doctor of Philosophy
in CREOL, The College of Optics and Photonics
at the University of Central Florida
Orlando, Florida

Spring Term
2022

Major Professor: Ivan Divliansky

ABSTRACT

This dissertation explores a new method for creating holographic phase masks (HPMs), which are phase transforming optical elements holographically recorded in photosensitive glass. This novel hologram recording method allows for the fast production of HPMs of any complexity, as opposed to the traditional multistep process, which includes the design and fabrication of a master phase mask operating in the UV region before the holographic recording step.

We holographically recorded transmissive HPMs that are physically robust (they are recorded in a silicate glass volume), can handle tens of kilowatts of continuous wave (CW) laser power, are un-erasable, user defined, require no power to operate, can work over a wavelength band ranging from 350 to 2500 nm, and can modify the wavefront of narrow line or broad band coherent sources. The HPMs can be wavelength-tunable by angular adjustment over tens or even hundreds of nanometers.

The HPMs incorporate the phase information in the bulk of a volume Bragg grating (VBG) resulting in only a single diffraction order and up to 100% diffraction efficiency. Recording in thick photosensitive medium also enables the multiplexing of HPMs in a single monolithic element. While these HPMs are physically overlapped in the space, they provide independent phase profiles, efficiencies, spectral and angular acceptances. Multiplexing HPMs allows splitting or combining of multiple beams while affecting their wavefronts individually.

We also developed a new holographic phase mask of reflective-type. This device provides us the ability of recording RBGs with transversely shifted parts in the larger aperture which upon reconstruction will produce different phases to different parts of the diffracted beam. RBG's diffraction spectrum possesses a very narrow bandwidth, and the holographic recording technique allows to multiplex multiple gratings into a single volume of PTR glass.

If each of these Bragg wavelengths is assigned with a specific spatial mode, it can be achieved simultaneous spatial and spectral multiplexing.

As a separate research topic, we look at how holographic optical elements (HOEs) can be used for improving the capabilities of the existing generation of head-up displays (HUDs), resulting in smaller, lighter units with a larger eye-box. Currently, surface relief gratings recorded in photosensitive polymers that are susceptible to the environmental conditions are used in HOE-based HUDs. This has an impact on their reliability and overall lifespan. We investigated a specific holographically recorded in the volume of photo-thermo-refractive glass transmissive gratings that generated multiple diffracted beams due to their operation in Raman-Nath regime. The Raman Nath gratings were successfully used to create an array of images because in augmented reality systems, this approach can be used to enhance the size of the exit pupil. These image splitting elements, due to the features of PTR glass, have a great resistance to temperature gradients, mechanical shocks, vibrations, and laser radiation.

ACKNOWLEDGMENTS

TABLE OF CONTENTS

LIST OF FIGURES

CHAPTER 1: INTRODUCTION

1.1   <u>Objective</u>

Laser beam shape control is used for many applications where a non-Gaussian beam is desired. Some examples of such applications are material processing[1-3], optical tweezers [4], optical communications [5-7], acceleration and trapping [8], biological imaging [9], and quantum information processing [10,11]. Beam shaping is typically performed by applying a specific phase profile to the beam, which can be accomplished by a variety of methods, including phase masks [12,13], adaptive optics [14,15], and spatial light modulators (SLMs) [16,17]. These techniques generally rely on complex optical elements to create the necessary phase distribution. Because the phase retardation at any given point is wavelength dependent, these techniques are naturally narrowband and, with the exception of SLMs and deformable mirrors, are not capable of changing the phase pattern at will. This specific spectral feature limits their application in broadband laser systems. Moreover, in the case of surface structured phase elements, the complex surface shape makes them sensitive to contaminations and impedes their use in high power laser systems.

A method of phase mask fabrication that produces masks suitable for use in high power systems is based on inducing a refractive index change in the bulk of a photosensitive medium, as demonstrated in Ref. [18]. Contrary to surface phase masks, such volume phase mask has plane polished surfaces that results in high resistance to surface contaminants. The photosensitive medium used was photo-thermo-refractive (PTR) glass [19], which has low absorption in the visible and near IR spectral regions (about $10^{-4}\ cm^{-1}$) and high tolerance to pulsed and CW laser radiation. However, even though recorded in the volume of a glass, these phase masks are still narrowband and are not wavelength tunable.

The absence of tunability of a volume phase mask was overcome when it was incorporated into a volume Bragg grating (VBG) [20]. VBGs are generally produced by recording an interference pattern of two collimated beams in the bulk of a photosensitive medium. The VBG diffracts an optical beam if the wavelength and angle of incidence correspond to the Bragg condition [21]. Changing the angle of incidence therefore results in tuning the diffracted wavelength. As discussed in Ref. [20], placing a conventional phase mask (master phase mask) designed for a UV wavelength into one of the recording beams results in the creation of a transmitting VBG with unusual properties. Specifically, the phase profile of the diffracted beam is identical to the phase profile in the recording UV beam produced by the master phase mask, regardless of the diffracted wavelength. Thus, this VBG acts as a tunable holographic phase mask (HPM). However, it is still a narrowband element.

The first approach for extending the operating bandwidth of HPMs was demonstrated in Ref. [22]. This work capitalized on the angular dispersion compensation produced by a system of two surface diffraction gratings with a single VBG placed between them [23]. It was shown that a transmitting VBG and a surface grating with a period twice as large as the VBG have the same angular dispersion. This means that if collimated broadband beam is diffracted by the first surface grating, , all its spectral components would satisfy the Bragg condition of the VBG for and would be diffracted, albeit in an angular fan. When this angular fan is launched to the second surface grating, all spectral components would be diffracted again, this time into a common angle. Thus, after three sequential diffractions, the broadband beam would be collimated while having a lateral spectral chirp. . It was found that the HPM incorporated into such a three-grating-system [22] became achromatic over a spectral range exceeding 1000 nm, enabling applications such as femtosecond broadband beam conversion from TEM_{00} to TEM_{11}.

A simplification of broadband HPM was achieved by utilizing VBGs with large periods [24], enabling the elimination of the surface gratings used in Ref. [22] due to the large spectral

acceptance of the VBGs. Specifically, the spectral selectivity of VBGs recorded in PTR glass can reach tens of nanometers for grating periods on the order of several microns and thicknesses of a few millimeters. Such HPMs were recorded and mode conversion for femtosecond beams with spectral width of 30 nm was demonstrated. This result demonstrated the ability to produce monolithic phase masks operating with high power broadband laser beams. The residual problem of this technology is the long time required for design, fabrication, and testing of the master phase mask for the VBG recording wavelength followed by optimization of the HPM recording process.

The objective of the present work is to address this final limitation and develop a versatile production technology that rapidly and inexpensively produces complex holographic phase masks recorded in PTR glass, and to show their applicability to a wide variety of applications.

1.2   Historical Background

Shaping light dates back in history almost as far as the invention of the laser itself, more than half a century ago [25,26]. Structured light was done first by manipulating the laser resonator properties adjusting the mirror size and radius of curvature such that the emitted beam had the desired transverse profile [27]. Shaping light external to the laser resonator using complex optical elements was also studied for decades [1-3] in the late 1980s and early 1990s. Historically, the development in this field can be traced to the advances in microelectronics and computing capability. These advances have been driven by fabrication techniques such as lithography, however, even the most recent advanced fabrication tools have their challenges and limitations.

The change of the intensity and the phase of a light field started with demonstrating spatial mode control by amplitude modulation[4] , then by phase filtering [5], and by the

3

combination of controlling light's spin and orbital angular momentum [6,28]. Spatially structured light refers to the ability to control light spatial fields in amplitude (intensity), phase (wavefront) and polarization [26]. Spatial modes which are solutions of the electromagnetic wave equation have always been in the focus of interest of optical researchers. The solutions are described by electromagnetic light fields that are transverse to the light propagation direction. Some well-known spatial modal distributions are Gaussian, Hermit-Gaussian (HG), Laguerre-Gaussian (LG), Bessel-Gaussian (BG), and Airy-Gaussian (AG) modes, which have found numerous practical applications [26].

In 1992, Allen et al. recognized that as light beams travel through space, if the phase structure rotates (i.e., a spiral phase profile), the light carries orbital angular momentum (OAM) equivalent to $l\hbar$ per photon (where l is an integer number) [29]. The beams that carry OAM are referred to as vortex beams and can be described by LG or BG modes [26,27]. It has been about 30 years since the beginning of generation and manipulation of optical vortices [30]. The use of spatial modes is considered a new degree of freedom for light to further increase the information transfer capacity [7]. Various methods for generation of such spatial modes have been developed throughout the years. Interferometric approaches, including diffractive elements or lithography-produced gratings are classical ways of beam shaping. In this work, we use holography recording approach to create the holographic optical elements in PTR glass for wavefront shaping.

1.3   Holographic Optical Elements

Holographic optical elements (HOE) can be used to transform an optical wavefront in the same manner as conventional optical elements. A major advantage of HOEs over conventional optical elements is that their function is independent of the substrate geometry.

4

In addition, since they can be produced on thin substrates, they are quite light, even for large apertures. Another advantage is that several holograms can be recorded in the same substrate by spatial multiplexing [31]. We can distinct two types of holographic optical elements - volume Bragg gratings (VBGs) and holographic phase masks (HPMs) which are also strongly related to each other. VBGs and HPMs are introduced in the following sections and will be discussed in more details in the next chapters.

1.3.1   Volume Bragg Gratings

William Bragg in 1915 used the scattered x-ray light from a crystal to extract the crystal's lattice structure information [32]. He found that at particular angle, the light was strongly diffracted by the crystal. This condition is called resonant condition or Bragg condition. The optical (longer than x-rays wavelengths) analog of the crystal structure is the so called "volume hologram". Such holograms are recorded in photosensitive materials be exposing them to the interference pattern (fringe pattern) created by overlapping laser beams. The spatial light modulation upon recording is converted to refractive index modulation and this creates the volume Bragg grating (VBG).

We record VBGs inside photosensitive PTR glass using holographic recording approach of interference of two collimated UV laser beams. Then thermal treatment is used to produce permanent refractive index modulation throughout the volume of the glass plate. When a beam incident on the VBG structure fulfils the Bragg condition, it is diffracted. Unlike surface Bragg grating which has different diffraction orders (Eq. 1-1), there is only one order of diffraction for volume Bragg gratings. When light passes through a typical surface grating, it diffracts into multiple orders (directions).

$$(\sin \theta_i + \sin \theta_m) = m\lambda/n\Lambda \qquad (1\text{-}1)$$

where, θ_i and θ_m represent the incident angle and diffracted angles at different orders of m, n is the material's refractive index, and Λ is the periodicity of grating.

In general, the volume Bragg grating properties are determined by the recording wavelength, angle of interference, and the refractive index modulation of the recording material. When using collimated laser beams, the recorded VBGs are uniform but there are techniques which produce more complex volume gratings and which will be discussed in chapter 2.

Kogelnik [21] in 1969 described the diffraction properties of a volume grating. He developed the first model of a uniform volume Bragg grating based on coupled wave theory (CWT). He applied the coupled wave theory to analyze the performance of thick transmission and reflection Bragg holograms. The geometry of recording of and propagation through a recording material with refractive index of n and thickness t with the period of grating Λ is shown in Fig. 1.3. Two recording beams of reference, R, and signal , S, beams with incident angles of θ_{iw1} and θ_{iw2} are interfered into the volume of the photosensitive material and VBG is made by recording of the interference fringes that create a corresponding refractive index modulation inside the medium. The gratings in the figure are tilted by an angle of θ_{tilt} with respect to the normal vector of the sample surface. The incoming reading beam is I and the diffracted beam which is the outgoing signal wave is d. k_i and k_d are the propagation vectors of I and waves respectively. k_d is diffracted by the grating and related to k_i and the grating vector K_G by [21]

$$k_d = k_i - K_G \qquad (1\text{-}2)$$

Particular properties of volume holograms are their high diffraction efficiency in only one diffraction order, and the angular/wavelength dependence of the diffraction efficiency to the incident light deviation from the Bragg angle or when its wavelength is changed. Accordingly,

to evaluate the performance of a VBG, there are three main parameters: diffraction efficiency(η), wavelength selectivity ($\Delta\lambda_{HWFZ}$) and angular selectivity($\Delta\theta_{HWFZ}$).

Volume Bragg gratings (VBGs) are considered to be spectral and angular selectors with highly adjustable parameters. The peak diffraction efficiency(η_0), angular selectivity($\Delta\theta$), and spectral selectivity ($\Delta\lambda$) of a VBG depends on its thickness(t), refractive index modulation (δn) and the angle of incidence in the medium(θ_i).

VBGs are typically divided into transmission Bragg gratings (TBGs) and reflection Bragg gratings (RBGs).
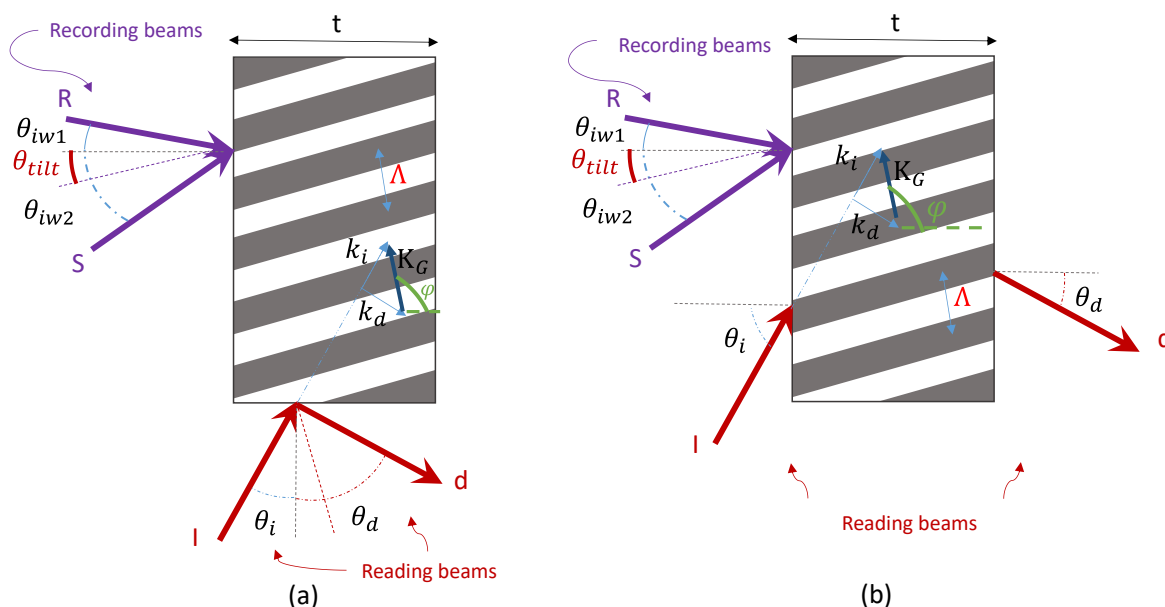
Figure 1-1 Schematic of writing and reading Bragg gratings (a) Reflective Bragg grating (b) Transmissive Bragg grating

1.3.1.1 *Reflective Bragg Grating*

In the case of Reflective Bragg gratings, the incoming light that matches the Bragg condition reflects back to the same side of the recording material (Fig. 1-1(a)). The incident angle is θ_i and the tilt angle of grating inside the volume of the medium is θ_{tilt}. Resonant diffraction arise at the Bragg condition which is defined by Eq. 1-2.

$$\lambda_{RBG} = 2n\Lambda\cos(\theta_i + \theta_{tilt}) \tag{1-3}$$

where, Λ is the period of the VBG and λ_{RBG} is the wavelength of the incident light on the RBG.

1.3.1.1.1 Spectral and Angular Selectivity

In particular, RBGs are narrow wavelength filters compare to transmissive Bragg gratings. For instance, the full-width-half-maximum ($FWHM$) of spectral selectivity of RBGs can be designed to reach down between $0.02 - 2\ nm$. They have typical angular acceptance of more than $10\ mrad$ all the way up to$100\ mrad$.

For an RBG, the peak diffraction efficiency can be greater than >99.9% and is calculated by[21,33]

$$\eta_0 = \tanh\frac{\pi t \delta n}{\lambda_0 |\cos\theta_m^*|} \tag{1-4}$$

where, t is the thickness of RBG, δn is the refractive index modulation, λ_0 is the central wavelength of the incident beam and $\theta_i = \theta_m^*$ is the incident Bragg angle. The half-width-first-zero ($HWFZ$) spectral width is given by,

$$\delta\lambda^{HWFZ} = \frac{\lambda_0\left(\left(\tanh^{-1}\sqrt{\eta_0}\right)^2 + \pi^2\right)^{1/2}}{\pi f t} \tag{1-5}$$

where, $f = \frac{1}{\Lambda}$ is the spatial frequency. The angular selectivity can be derived from the Bragg angle,

$$\delta\theta_m^{HWFZ} = \left(\tan^2\theta_m^* + \frac{2\delta\lambda^{HWFZ}}{\lambda_0}\right)^{1/2} - \tan\theta_m^* \tag{1-6}$$

Accordingly, using the above equations, an RBG can be designed for a desired diffraction efficiency and spectral selectivity. Therefore, for a given diffraction efficiency, spectral selectivity and central wavelength, we are able to calculate the required thickness and refractive index modulation of the particular RBG. For example for a beam with an incident angle of 10°, wavelength of 1064 nm, diffracted by a 1 mm thick not tilted RBG and an index modulation of 900 ppm, the angular and spectral selectivity diagrams are shown in Figs. 1-2 (a

and b) respectively. The FWHM of the angular selectivity is approximately 6.24 mrad and the

FWHM of the spectral selectivity is close to 1 nm.
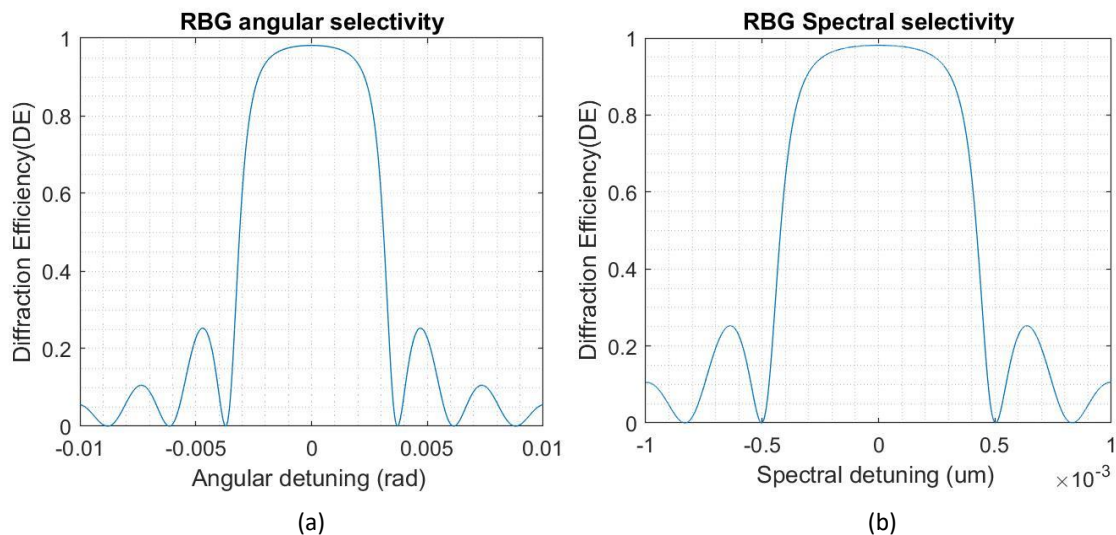
Figure 1-2 (a) Spectral and (b) angular response for an RBG (1mm thickness, tilt 0 degrees, index modulation of 900 ppm). The beam incident angle is 10°, and its wavelength is 1064 nm Transmissive Bragg Grating

1.3.1.2   *Transmissive Bragg Grating*

In the case of transmissive Bragg grating, the incident light is that satisfies the Bragg

conditions one side of the sample while the diffracted beam is on the opposite side (Fig. 1.1b).

The incident angle is θ_i and the tilt angle of the grating inside the volume of the medium is

θ_{tilt}. Resonant diffraction arises at the Bragg condition which is defined by Eqs. 1-7.

$$\lambda_{TBG} = 2n\Lambda\sin\left(\theta_i + \theta_{tilt}\right) \qquad (1\text{-}7)$$

where, Λ is the period of the VBG and λ_{TBG} is the wavelength of incident light.

1.3.1.2.1 Spectral and Angular Selectivity

In contrast to RBGs, TBGs have broad spectral selectivity starting at 0.3 up to $20\ nm$,

while having narrow angular acceptance between 0.1 to $10\ mrad$, which makes them useful

as narrow angular filters. Their diffraction efficiency can reach up to 100% and is calculated

using,

9

$$\eta = \sin^2(\pi n t / \lambda \cos \theta_i) \qquad (1\text{-}8)$$

Angular selectivity at half width of fist zero ($HWFZ$) level $\delta\theta_m^{HWFZ}$, is the angle between the central maximum and the first minimum at the diffraction efficiency curve. For VBGs with 100% diffraction efficiency the $HWFZ$ angular selectivity is given by:

$$\delta\theta_m^{HWFZ} = \frac{\sqrt{3}}{2ft_0} \qquad (1\text{-}9)$$

The spectral selectivity of TBGs, has the same structure as the angular selectivity due to their linear interrelationship as described by Eq. (1-10), which is the differential form of the Bragg condition equation [34]. The angular selectivity for transmitting gratings with 100% diffraction efficiency could be derived by Eq. (1-11):

$$\frac{\Delta\theta_m}{\Delta\lambda} = \frac{f}{2n_{av}F_{\pi/2}} \qquad (1\text{-}10)$$

$$\delta\lambda^{HWFZ} = \frac{\sqrt{3}n_{av}F_{\pi/2}}{f^2 t_0} \qquad (1\text{-}11)$$

where, f is the spatial frequency, n_{av} is the average refractive index of a medium, t_0 is the minimum thickness of the grating and $F_{\pi/2}$ inclination factor of normal transmitting grating ($\varphi = \pm\pi/2$).

Figs. 1-3(a and b) show the angular and spectral selectivities of a non-tilted TBG with 1 mm thickness and an index modulation of 500 ppm for a beam with an incident angle of 10° at 1064 nm, sample. The FWHM of angular selectivity is about 2.4 $mrad$ and the FWHM of spectral selectivity is about 22.6 nm.
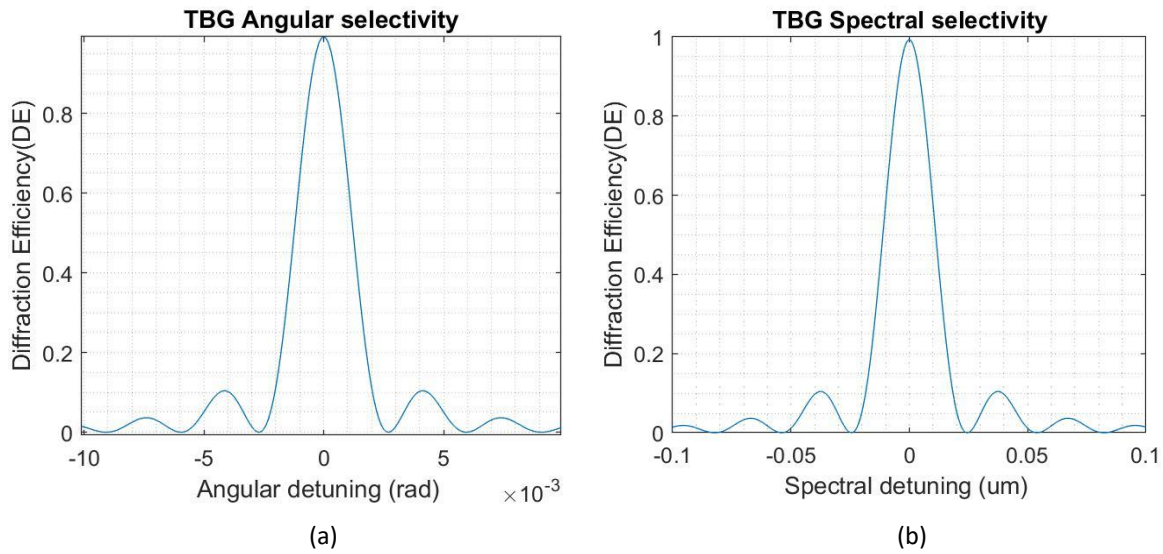
Figure 1-3 (a) Spectral and (b) angular response for a 1 mm thick TBG, tilt angle of of zero with index modulation is 500 ppm TBG. The incident angle of beam is 10° at 1064 nm

1.3.2 Holographic Phase Masks (HPMs)

Conventional optical phase masks are limited to use at a specific wavelength. To make a single phase mask operate at different wavelengths one need to encode the phase masks profile into a volume Bragg grating, which is called holographic phase masks (HPMs). Such HPMs can be used with narrow or broad spectra depending on their design and produce the desired phase profile in the diffracted beam, as long as the Bragg condition of the VBG is met for the given wavelength. The HPMs being recorded into VBGs have the diffraction properties of regular VBGs; they can diffract up to 100% of a beam to a single order and have specific angular and wavelength selectivities.

1.4 Holographic Recording Materials

To record holographic optical element, a material that is photosensitive is required and there is a wide variety of photosensitive materials that can be used for the purpose [35,36]. In most cases, volume Bragg gratings are made by recording interference fringes that create the

11

corresponding refractive index modulation inside a medium. Therefore, the recording materials require to have enough spatial resolution that can encode gratings with particular periods. Since VBGs are recorded by interference of light, the photosensitivity of the material is very important because it determines the duration of the recording. Another important property of the recording material is the material's dynamic range which provides the maximum refractive index variation. The dynamic range therefore determines the maximum number of volume gratings that can be multiplexed and as a result the thickness of the recording material. Since volume Bragg gratings are widely used in high power laser applications, the optical damage threshold of the material is also a significant property.

The most common recording materials are dichromated gelatins, photopolymers, photorefractive crystals, photosensitive fibers, and photo-thermo-refractive (PTR) glass. PTR glass is UV-photosensitive glass that has resolution below $50\ nm$ and is capable of handling high power laser radiation with measured damage threshold for 8 ns laser pulses at $1064\ nm$ of $40\ J/cm^2$ [37-39]. Another important advantage of the PTR glass is its very low losses which are on the order of $10^{-5}\ cm^{-1}$ at $1\ \mu m$. Therefore, we can state that PTR glass is very suitable material for recording volume Bragg gratings and in general for holographic phase recording.

In order to record a hologram into PTR glass, a two-step hologram formation process that includes UV exposure and thermal treatment is followed. The PTR glass is a $Na_2O - ZnO - Al_2O_3 - SiO_2$ glass doped with silver (Ag), cerium (Ce), and fluorine (F) atoms. First, the glass is exposed with UV light with wavelength between $280\ nm$ to $350\ nm$. The exposure causes photo-reduction of silver ions (Ag^+) to silver atoms (Ag). At this stage there is no significant changes in the optical properties of the glass. Then, the glass is subjected to 2-stage heat treatment process. In the first stage, silver-containing clusters are created by the increased mobility of the silver atoms. They act as the nucleation for the growth of sodium fluoride, NaF

12

crystals during the second thermal phase. The interaction of this NaF nano-crystals with their surrounding inside the glass result in decreasing the refractive index of the exposed parts. The refractive index modulation δn can be as high as $1.5 \times 10^{-3} (1500\ ppm)$ [40].

CHAPTER 2: TRANSMISSIVE HOLOGRAPHIC PHASE MASKS

2.1   Holographic Phase Mask (HPM) Recording and Testing

The same basic approach as in Ref. [20] was applied for HPM recording, wherein two collimated beams were interfered, with the object beam containing the phase element required to create the mask. In contrast to the previous work, where a conventional master phase mask was placed into one arm of the holographic recording setup, a UV operating SLM is used here to generate the desired spatial phase profile into the object beam. As SLMs are active computer-controlled devices that can be programmed to generate nearly any desired phase profile, the fabrication challenges related to producing predetermined phase masks are alleviated. Therefore, by using an SLM for direct profiling of the phase of one of the hologram's recording beams, one can generate a wide variety of HPMs in a flexible, fast and simple way. The holographic setup is presented in Fig. 2-1. A Gaussian beam from a He-Cd laser at 325 nm (KIMMON KOHA Co.-IK3501R-G) is spatially filtered and expanded by lenses L1, L2, and a pinhole PH. Then it is launched to a beam splitter (BS1) that produces object and reference beams. The object beam is directed to an SLM (HOLOEYE PLUTO-2-UV-099) by a mirror M3. Then it is reflected from the liquid crystal SLM which introduces a predetermined spatial profile of phase incursion. A 4-f system (L3, L4, and PH) spatially filters the beam and images the plane of the SLM to the recording plane inside of a PTR glass plate. The SLM has a resolution of 1920×1080 pixels, each with a rectangular area of 8×8 μm^2. Each pixel acts as an individually programmable phase shifter in an interval between 0 and 2π. The reference beam is redirected by mirrors M1, M2, and M4. Its power is controlled by a polarizer (P). To combine the two beams, an additional beam splitter (BS2) was used. Inclination of the mirror M4 controls a converging angle between object and reference beams. While this design causes

power loss, it enables varying converging angles (including small ones) without increasing the recording setup size. Note that while the path lengths of the arms are different, the difference is within the 1 m coherence length of the laser. The HPM thus recorded will have an induced phase profile determined by the phase pattern incurred on the SLM. PTR glass wafers were exposed in this manner and thermally developed to obtain the permanent refractive index modulation required for a predetermined diffraction efficiency [19].
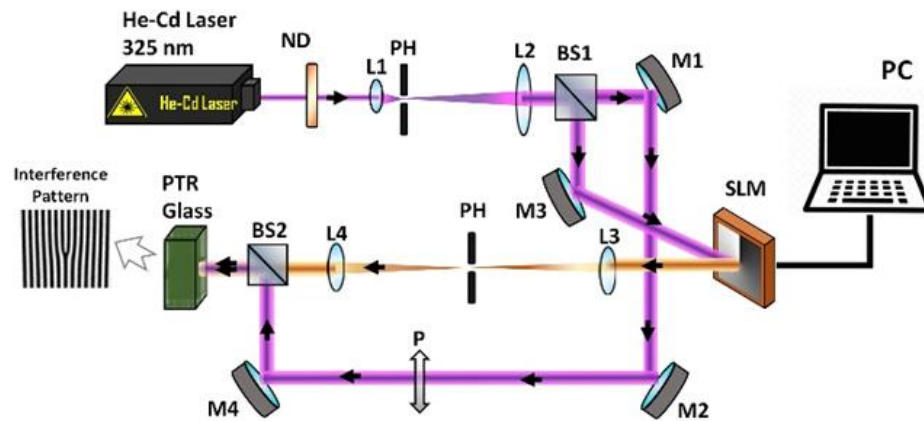
Figure 2-1 Schematic diagram of the experimental holographic setup for encoding phase masks using an SLM. (ND: Neutral Density Filter, L1: UV Lens with f1=25 mm; PH: Pinhole; L2: UV Lens with f2=150 mm; BS: Beam Splitter, M1, M2, M3, M4: UV Mirrors; L3, L4: UV Lens with f3= f4=150 mm; P: Polarizer; SLM: Spatial Light Modulator, PTR Glass: Photo-Thermo-Refractive Glass).

The characterization of the recorded HPMs was done using the characterization setup depicted in Fig. 2-2 Three lasers were used for characterization. First, the recording He-Cd laser operating at 325 nm was used for characterization at the recording wavelength. Second, a He-Ne laser (Melles Griot 05-LMP-141) and a laser diode (Newport-LQA1066-150E) were used for characterization at 633 and 1064 nm, respectively. A single transverse mode beam was spatially filtered and expanded by lenses L1 and L2 and a pinhole PH. The expanded Gaussian beam was launched to an HPM under test that was mounted on a high precision translation/rotation stage. Depending on wavelength and angle of incidence, the beam is split to transmitted and diffracted orders. The far field of a diffracted beam was imaged onto a CCD

15

camera (Imaging Source-DMK 72BUC02) by the L3 lens. The image was digitized to a 2D

intensity profile using IC Imaging Control Software.
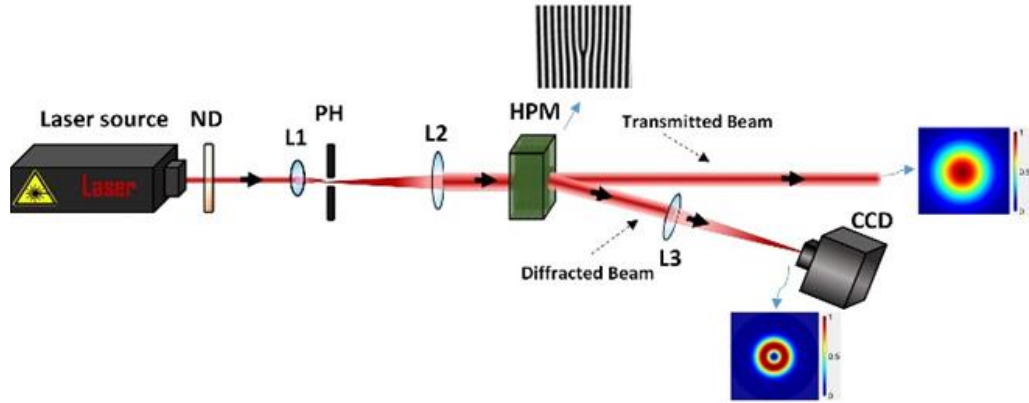
Figure 2-2 Schematic diagram of the HPM beam conversion characterization setup. (ND: Neutral Density Filter; PH: Pinhole; HPM: Holographic Phase Mask; L1: Lens1 with f1 =25 mm, L2: Lens2 with f2=150 mm, L3: Lens3 with f3=250 mm, CCD: Charge-Coupled-Device Camera).

2.2   Mode Conversion by Transmissive Holographic Phase Masks (THPM)

The procedure of holographic phase masks recording includes the following steps.

First, the desired phase profile is determined. Second, the SLM is programmed to generate the

desired phase profile at the recording wavelength. Third, the recording object beam is

characterized to verify that the phase profile generated is acceptable. Fourth, the HPM is

recorded and characterized.
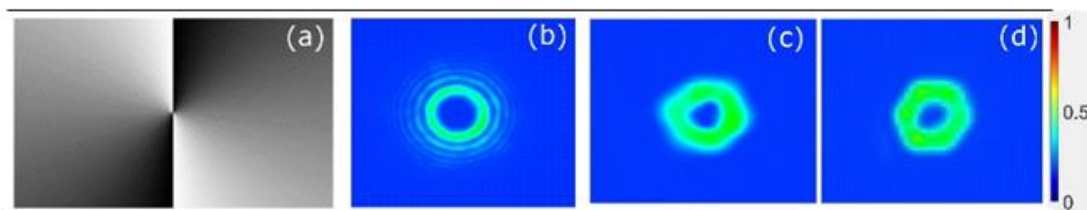
Figure 2-3 (a) Modelled LG02 mode phase profile with radial phase incursion from 0 to π; (b) intensity profile in far field for a 325 nm beam reflected by the SLM; (c) intensity profile of diffracted by the HPM 633 nm beam; (d) intensity profile of diffracted by the same HPM 1064 nm beam after tuned to the corresponding Bragg angle.

An illustration of the procedure is shown in Fig.2-3, where a Gaussian beam with a

plane phase profile is converted to the LG_{02} mode. The required phase profile is characterized

16

by constant phase incursion in any radial direction and linear increase of phase incursion from zero to π in azimuthal direction (white-to black in Fig. 2-3(a)).

The helically phased beams carry optical angular momentum (OAM) and are related to Laguerre-Gaussian (LG) modes, which are radially symmetric and have an associated azimuthal phase term. For OAM-carrying beams, a simple expression of the scalar LG beam can be written as [27],

$$
\begin{aligned}
u_{p,l}^{LG}(r,\varphi,z) = \left(\frac{2p!}{\pi(p+|l|)!}\right)^{\frac{1}{2}} \left(\frac{1}{\omega(z)}\right) \left[\frac{r\sqrt{2}}{\omega(z)}\right]^{|l|} &\times \exp\left[-\frac{ik_0 r^2}{2R(z)}\right] \exp\left[-\frac{r^2}{\omega(z)^2}\right] \times \\
L_l^p\left(\frac{2r^2}{\omega(z)^2}\right) \exp\left[-i(2p+|l|+1)\tan^{-1}\left(\frac{z}{z_R}\right)\right],
\end{aligned}
\tag{2-1}
$$

where r is the radius, φ is the azimuthal angle, z is the axial distance, $R(z) = (z^2 + z_0^2)/z$ is the radius of curvature of the wavefront, ω_0 is the minimum beam radius at $z = 0$, $z_0 = k\omega_0^2/2$, is the Rayleigh range, k is the wave number, $\omega(z) = \omega_0\sqrt{1 + (z/z_0)^2}$ is the beam waist at distance z, and $(2p + |l| + 1)\tan^{-1}\left(\frac{z}{z_R}\right)$ is the Gouy phase shift. $L_l^p(x)$ is a generalized Laguerre polynomial with radial index l and azimuthal index p. The beam profile depends on the topological charge l of the beam:

$$
L_l^p(x) = (-1)^{|l|}\frac{d^{|l|}}{dx^{|l|}}L_{p+|l|}(x).
\tag{2-2}
$$

The far field intensity profile obtained for the recording beam at 325 nm after reflection from the SLM, shown in Fig. 3-3(b), is very close to the theoretical profile of LG_{02} mode. After exposure and thermal development, the HPM was recorded in a PTR glass plate. Placing the HPM to the setup shown in Fig. 2 and tuning it to the Bragg angle for 633 nm, a strong diffracted beam was observed, as shown in Fig. 3(c). One can see that the resulting beam profile also closely matches the expected LG_{02} mode. Tuning the HPM for 1064 nm resulted in the beam profile shown in Fig. 3(d), which also matches the expected LG_{02} mode. Consequently, an HPM provides mode conversion for any wavelength when an incident beam satisfies the Bragg condition.

It should be noted that HPMs can be used to create beam profiles other than Laguerre-Gaussian or Hermite-Gaussian modes. Figure 4 demonstrates the conversion of a Gaussian beam to an Airy beam [26], with Fig. 4(a) showing the phase projected on the SLM and encoded in the HPM, Fig. 4(b) showing recording beam after reflection by the SLM, and Figs. 4(c) and 4(d) showing Airy beams produced by the HPM at 633 and 1064 nm, respectively.
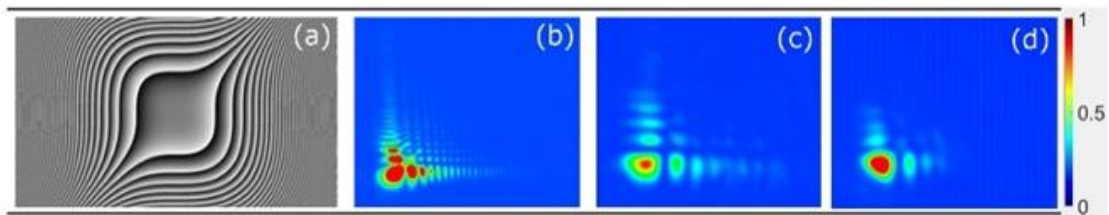
Figure 2-4 (a) Modelled phase profiles for 325 nm for conversion to Airy beam, (b) intensity profile in far field for a 325 nm beam reflected by SLM, (c) and (d) and beams at 633 nm and 1064 nm diffracted by the HPM upon tuning to the corresponding Bragg angles.

Figure 5 is another example which demonstrates the conversion of a Gaussian to a Bessel beam [27]. Figs. 5(c, d) and 5(f, g) are clear illustrations of the capability of the HPMs. The converted beams match very well with the ones directly converted from the SLM regardless of whether one is in the non-diffracting regime or not.
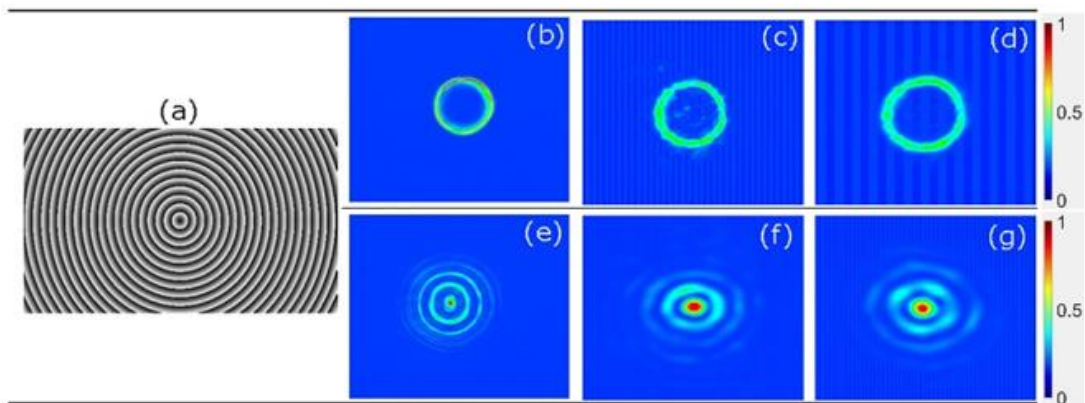
Figure 2-5 (a) Modelled axicon phase profile for 325 nm for conversion to Bessel beam; (b) far field intensity profile imaged after non-diffractive length using a 325 nm beam reflected from the SLM; (c) and (d) corresponding far field intensity profiles for beams diffracted by the same HPM at 633 and 1064 nm, respectively. (e) far field intensity profile imaged into the non-diffractive length using a 325 nm beam reflected from the SLM; (f) and (g) corresponding far field intensity profiles for beams diffracted by the same HPM at 633 and 1064 nm, respectively.
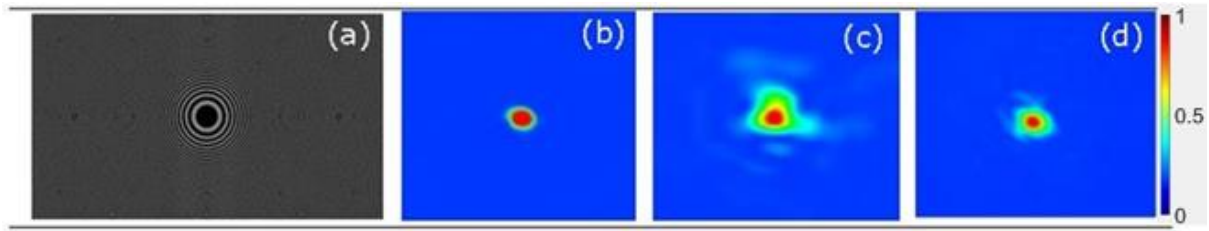
Figure 2-6 (a) Modelled phase profile of a Fresnel zone plate with focal length of 320 mm operating at 325 nm (b) intensity profile of focal spot in far field for a 325 nm beam reflected by SLM, (c) and (d) focal spots of beams at 633 nm with focal length 170 mm and 1064 nm with focal length 86 mm diffracted by the HPM upon tuning to the corresponding Bragg angles.

As a last example in this section, Fig. 6 shows the results of encoding a Fresnel zone plate as an HPM. Two such zone plates, with focal distances of 320 mm and 500 mm at 325 nm, respectively, were recorded as HPMs. The performance of the holographic lenses was characterized at 633 nm and 1064 nm and the corresponding focal lengths of 170 mm and 230 mm (at 633 nm) and 86 mm and 138 mm (at 1064 nm) were measured. Given that the focal length of a Fresnel zone plate is inversely proportional to the wavelength, the measured focal distances at 633 nm and at 1064 nm fit reasonably well to the theoretically predicted values of 164.3 mm and 256.7 mm (at 633 nm) and 97.7 mm and 152.7 mm (at 1064 nm). We attribute the difference either to the recording beam collimation quality or to a misalignment of the 4-f imaging system used in the recording setup. Both effects could introduce distortions of the grating pattern and therefore change the focal length of the lens.

In summary, a number of holographic mode convertors were recorded and tested. The observed results demonstrate the capabilities of the HPMs to reproduce practically any encoded phase profile. The HPMs recorded in PTR glass are neither programmable nor switchable, but they work at any wavelength where Bragg conditions for the corresponding TBG are satisfied. Furthermore, because they can be multiplexed as with standard TBGs, it is possible for a single optical element to convert a beam to different modes by angular tuning.

19

2.3   Top-Hat Holographic Phase Mask

Generation of top-hat beams that have uniform intensity distribution has numerous applications in various fields. We holographically recorded in PTR glass phase structures that upon diffraction create top-hat beams. The holographic setup is the same as the recording setup shown in Fig. 2-1, where either SLM or phase mask are used in the signal beam path. Two collimated beams were interfered, with the signal beam being transmited through either a UV operating phase mask (HOLOOR inc.) containing the top-hat converting spatial phase profile or an SLM (Holoeye PLUTO-2) displaying top-hat converting phase profile. The HPM thus recorded will work as a Gaussian to top-hat converting hologram in a manner similar to the one implemented into the phase mask or the SLM.

The top-hat HPM is characterized in the same way as the testing configuration shown in Fig. 2-2. A diode laser operating at 1064 nm with a beam size of $FW(1/e^2)$ 1.3 mm passes through two lenses L1 and L2 in order to be expanded to 4 mm. Then the expanded beam illuminates the HPM precisely around the top-hat phase pattern centrosymmetric. The incident Gaussian profile is shown in Fig. 2-8. The incident beam is diffracted at the Bragg angle of 9.5° with 95 percent diffraction efficiency after passing through the HPM (Fig. 2-7). To image the resulting beam cross section in far-field a Fourier lens was used. Using a lens with a focal length of 1000 mm produced a beam with size of 1.77 mm $(1/e^2)$, and when using a fast lens with a focal length of 100 mm the size was 160 μm. Figures. 2-9(a-c) and 2-10(a-c) present two-dimensional transformed top-hat beam profiles as well as one dimension horizontal and vertical profiles.
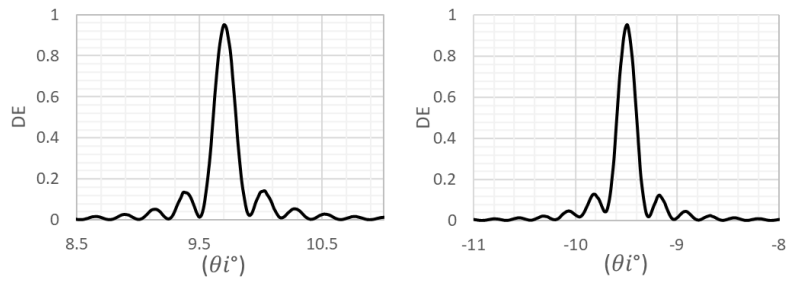
Figure 2-7 Diffraction efficiency of recorded top-hat HPM at 1064 nm with incident beam size of $FW\left(\frac{1}{e^2}\right) = 1.3\ mm$
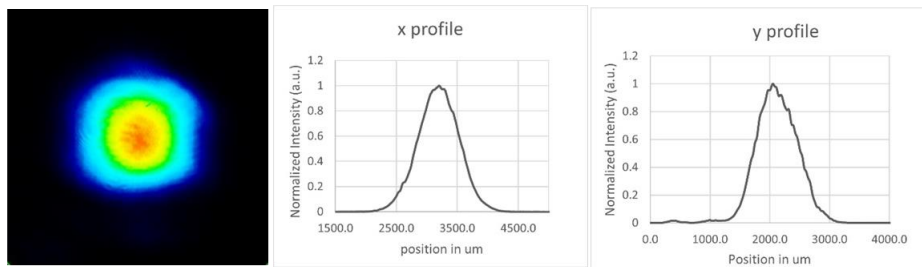
Figure 2-8 Incident Gaussian beam profile of diode laser at 1064 nm $FW\left(\frac{1}{e^2}\right) = 1.3\ mm$
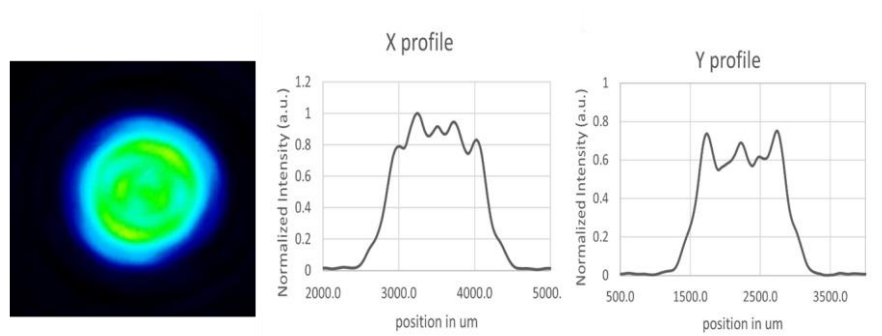
Figure 2-9 Measured far field top-hat beam profile generated by using the recorded top-hat HPM. (lens with 1000 mm focal length and top-hat beam size of $FW\left(\frac{1}{e^2}\right) = 1.77\ mm$).
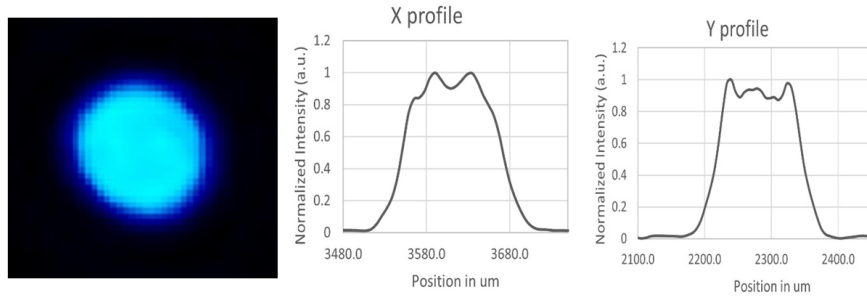
Figure 2-10 Measured far field top-hat beam profile generated by using the recorded top-hat HPM (lens with 100 mm focal length, top-hat beam size of $FW\left(\frac{1}{e^2}\right) = 160 \ \mu m$).

2.3.1 Theoretical Simulation of Top-Hat Beam Conversion

For efficient beam shaping, that is, how much the beam conversion is close to the ideal intensity distribution, the relation between the top-hat size and the diffraction limited spot size should be greater than 3 which is recommended by Holoor inc. phase mask developer. As an example, the diffraction limited spot size for a 4 mm beam at 1064 nm achieved by using a 100 mm is roughly $1.22\frac{\lambda}{D} * f \approx 32.45 \ \mu m$. As a result, the top-hat beam size generated by a top-hat HPM utilizing the same 100 mm lens exceeds $100 \ \mu m$.

The simulation results using the experimental specifications for an incident 4 mm Gaussian beam at 1064 nm and by implementing a 100 mm lens after the top-hat converting HPM are shown in Fig. 2-11. The transformed top-hat beam size is FW($1/e^2$)=160 μm, which is compatible with the previous section experimental data. Figures 2-12 and 2-13 show the output beam's 2-D and 1-D intensity beam profiles including graphs showing the beam evolution upon defocusing around the focal plane. The results reveal that a uniform intensity beam profile around the focal plane of a 100 mm lens requires less than 0.5 mm tolerance.
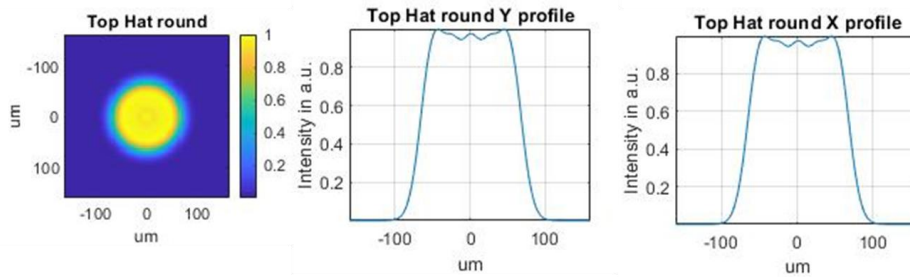
Figure 2-11 Simulation results of a top-hat beam conversion using 100 mm focal length lens(wavelength 1064 nm and 4 mm incident Gaussian beam), output top-hat beam size of $FW\left(\frac{1}{e^2}\right) = 160\ \mu m$
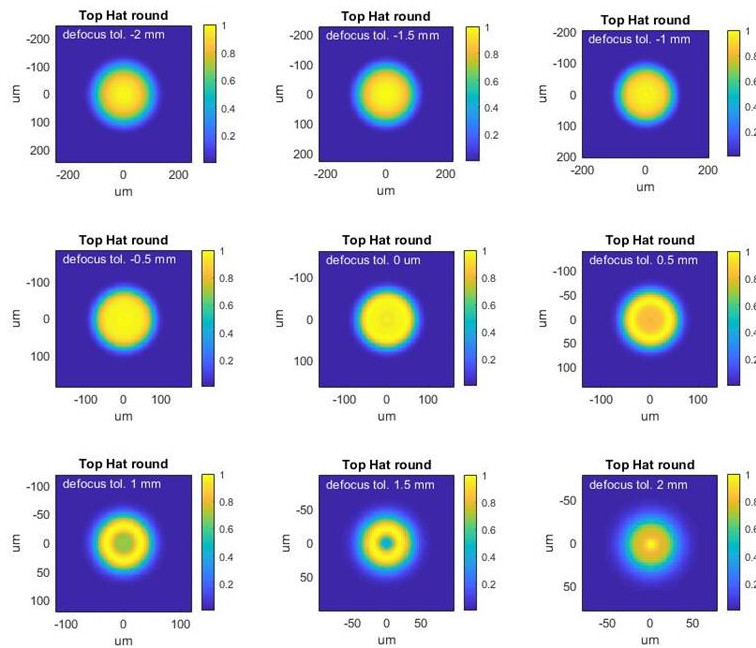
Figure 2-12 *Simulation results of 2D beam profile along defocusing the top-hat beam around the focal plane of a 100 mm focal length lens. Tolerance: < 5 mm (HOLOOR software)*
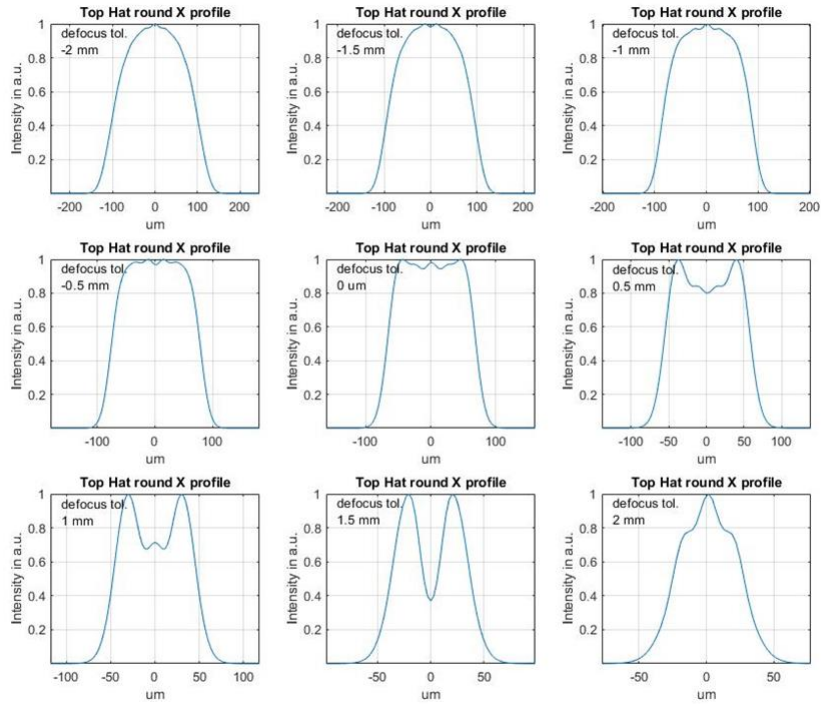
Figure 2-13 Simulation results of 1D beam profile along defocusing the top-hat beam around the focal plane of a 100 mm focal length lens. Tolerance: < 5 mm (HOLOOR software)

Therefore, in order to achieve a decent uniform top-hat intensity distribution, it is necessary to adjust the Fourier plane around the focal plane with minimum tolerance of defocusing.

2.4 Computer-Generated-Hologram HPMs

In computer-generated-holograms (CGHs), in fact the hologram pattern is numerically designed and optimized. The CGH capabilities and areas of applications have expanded significantly in the recent decade. CGHs are used in various applications such as three-dimensional (3-D) displays, projection, head mounted displays (HMD), augmented reality (AR), optical tweezers [41], and multi spot generations as well as encryptions .

Computer-generated holography can create any desired intensity pattern by modulating the wavefront of a light beam. Another advantage of holographic information storage is the

approach of information retrieval. The information can be extracted from the stored data by illuminating the memory plane and read out data at image plane at far field.

Computer-generated-hologram (CGH) allows any arbitrary light intensity distribution to be reconstructed, in contrast with conventional holography where only a physical wavefront of a real object can be recorded and then reconstructed. The hologram can be recorded on a film or other photosensitive material. CGHs are produced by a diffraction calculation that projects a 2D or 3D object on a virtual hologram plane on a computer. Conventional types of CGH can be printed by lithography on photoresist materials or by using an SLM. Here, we use a new approach of holographic recording CGH into PTR glass. For computing the holographic information of CGHs, different calculation methods have been developed, such as detour-phase hologram, Kinoform hologram and Iterative Fourier transform algorithm. There are three main steps for fabricating a computer-generated-hologram: 1- calculation of the phase dependences in the digital hologram; 2- encoding of the computed phase into the surface or volume of medium; 3- reconstruction of the desired intensity distribution at far field or the image plane of a lens. For calculating CGHs we used the Iterative Fourier transform algorithm (IFTA) followed by recording of the CGH into PTR glass.

2.4.1 Iterative Fourier Transform Algorithm

Iterative Fourier algorithm is a method capable of optimizing phase only Fourier holograms [42]. This algorithm (IFTA) was first proposed by Hirsch et al. [43] Independently, Gerchberg and Saxton [44] developed a phase-retrieval method using a similar algorithm and therefore IFTA is also called Gerchberg-Saxton algorithm.

In generating a phase only hologram, $H_p(x, y)$, the intensity of the reconstructed image must be proportional to the desired amplitude distribution $A(x, y)$, that is:

$$\mathcal{F}\{H_p(x,y)\} = \mathcal{F}\{ae^{-j\varphi}\} = A(x,y)e^{-j\phi(x,y)} \tag{2-3}$$

where, $\varphi(x,y)$ is the phase of the hologram, and $\phi(x,y)$ is the phase of the reconstructed image. In designing the phase-only CGH, we need to find a phase function $\phi(x,y)$ that will let $H_p(x,y)$ become a phase-only function. The IFTA is an algorithm searching for the best solution of $\phi(x,y)$.

The IFTA flowchart for generating a Fourier hologram is shown in Figure 2-14. The incoming beam was first modified with an initial phase pattern. The initial field is then transformed into a far-field intensity distribution using Fourier transform. At each iteration, the constraint is to obtain the desired intensity distribution in the far field. As a result, the inverse Fourier transform is used to translate the modified intensity distribution of the field in the Fourier domain back to the field in the incident domain. The resulting field is then used as the starting point for the next iteration. As a result, after several cycles, the far field intensity distribution approaches the target beam conversion. When IFTA only searches within a small region of phase functions set (unit cell), the solution is locally optimized. The reason for this localized calculation (unit cell) is that there are a huge number of variables which requires heavy computations which will take too long.
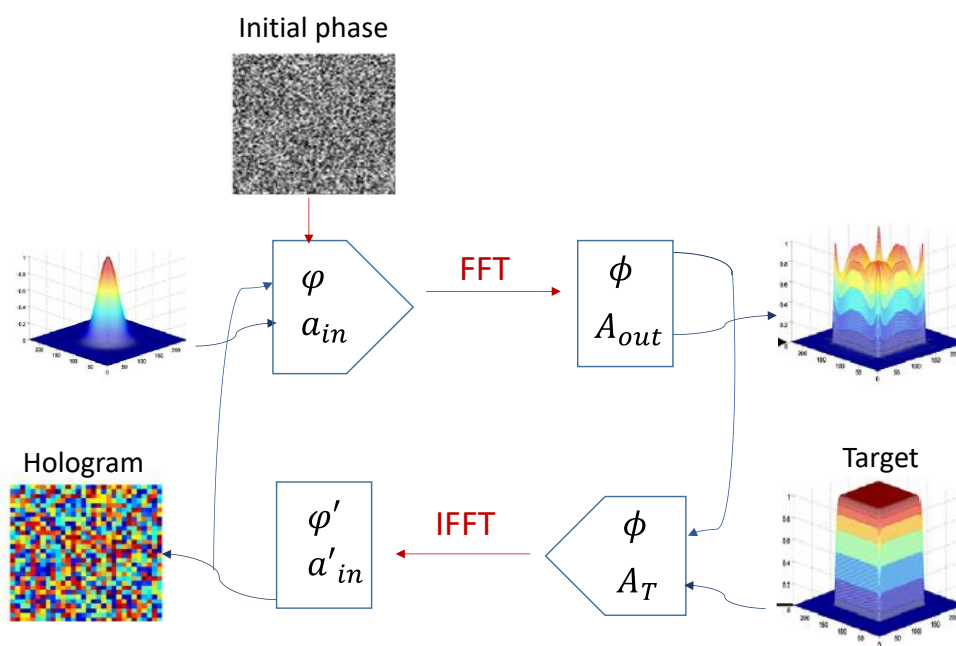
Figure 2-14 Flowchart of IFTA

For example, with 512×512 number of pixels and 256 phase levels, there are a total of $256^{512 \times 512}$ phase functions. In order to search for global optimization solution, additional algorithms must be included to the IFT algorithm. For calculating our CGH we used a commercially available IFTA software from HoloEye, Inc.

We used the previously described holographic setup to record the IFTA calculated CGHs into transmissive volume Bragg gratings. The CGH of the UCF logo (Fig. 2-15b), for example, was calculated and recorded into a TBG. The recorded HPM is reconstructed at far field using He-Ne laser (at 632 nm wavelength). Figure 2-15c depicts the experimental result.

There are many demands in various applications for beam shaping. Therefore, in order to produce the desired intensity profile the computer generated hologram approach is one of the best approach with its flexibility of computer design outcome and simple holographic recording. Our results demonstrated that CGHs can be encoded into an HPMs which brings an

27

additional and very power approach for generating arbitrary intensity distributions to the HPM capabilities.

(a) (b) (c)
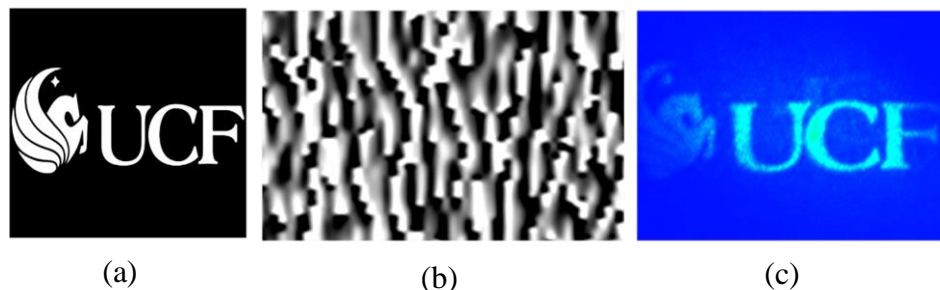
Figure 2-15 (a) Simulated profile of the UCF logo (b) Calculated CGH phase pattern (c) Experimental result of image generated by the recorded HPM with encoded computer generated hologram of the UCF logo

2.5 HPM Operation In High-Power Laser Beams

To demonstrate the high-power capabilities of the HPMs recorded in PTR glass, an HPM that converts a Gaussian beam to the LG_{08} mode was fabricated and illuminated with a Yb-doped fiber laser producing CW power between 50 W and 1 kW at 1070 nm (an IPG Photonics YLR-1000). The spectral width of the laser was approximately 5 nm (FWHM) and the laser beam diameter (FWHM) was 6 mm. The laser provided power densities from 0.35 to 3.5 kW/cm^2 and illuminated the sample at a $4°$ incidence angle. Figure 2-16 shows the conversion of a Gaussian beam to the LG_{08} mode at two different powers – 100 W and 1000 W. One can see that the converted mode profile closely matches the theoretically predicted one. To our knowledge, this is the first successful mode conversion using a holographic optical element at such power levels and power densities. It should be noted that, if needed, beam splitting into numerous beams, each with a different phase profile, could be achieved by using a multiplexed HPM.
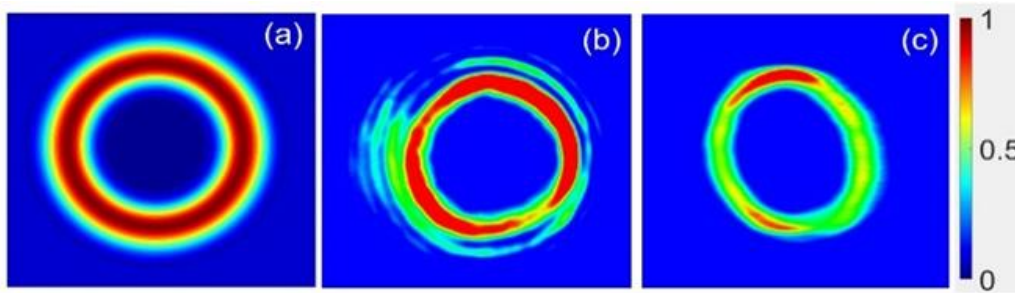
Figure 2-16 Intensity profiles of LG_{08} mode in far field; (a) theoretical; (b) and (c) experimental profiles of diffracted by the HPM 100 W and 1000 W beams, respectively.

2.6 Ultra-Short Pulse Laser Beam Mode Conversion

There are a variety of applications using ultra-short pulse lasers that require non-Gaussian beam profiles to achieve the intended results. Manipulating the transverse mode structure of ultra-fast laser systems to expand and improve their applicability is an area of active study [45-48]. Laser filamentation using femtosecond laser pulses has emerged as a new research direction and it was shown that vortex beams are better suited than Gaussian ones for such applications [46-48]. Phase elements fabricated by lithographic techniques on the surface of a transparent substrate are usually used for such mode conversions. However, such elements suffer from fast deterioration due to surface contamination and concentration of extreme electric fields at the edges of the surface structures. Moreover, they are monochromatic and cannot operate with broadband femtosecond laser pulses. In contrast, the HPMs produced by phase encoding of transmitting VBGs have the same spectral width that could be extended to tens of nanometers and, therefore, should provide mode conversion for femtosecond pulses.
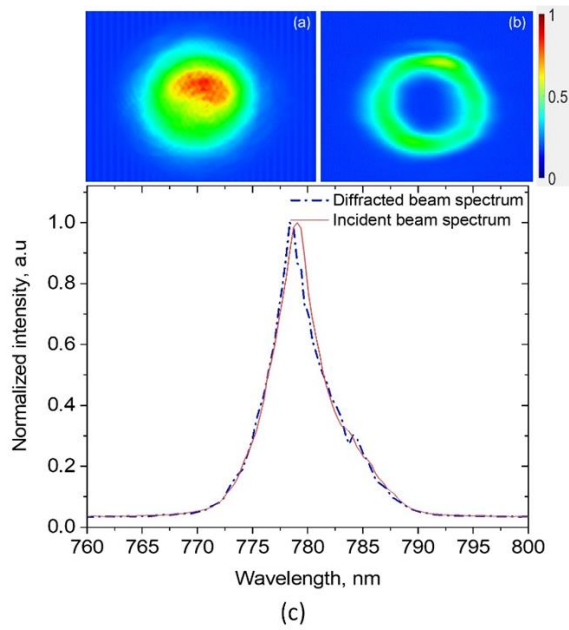
Figure 2-17 (a) Incident beam profile and (b) diffracted vortex beam profile of broadband femtosecond laser, (c) Incident and diffracted spectra.

To demonstrate the great potential of such broadband HPMs for wavefront modification of spectrally broad sources, a mode conversion using a vortex HPM was performed for a commercial femtosecond laser system (a Femtosecond Laser from IMRA, Inc.), with emission wavelength of 780 nm, spectral width of 17.2 nm (FWHM), and a pulse duration of 70 fs (FWHM). Fig. 2-17(a and b) show the incident and diffracted beam profiles produced by the HPM. Note that while HPMs do in general have some level of chromatic dispersion, which would normally result in blurring of the beam profile along the horizontal axis, the dispersion observed for this laser was negligible, as seen in Fig. 2-18(c). Furthermore, as shown in Fig. 2-18(c), no spectral components were lost after the incident beam was diffracted by the HPM.

The results demonstrate that HPM diffracts and changes the phase of sources having spectral widths of tens of nanometers, which show their enormous potential and applicability in ultra-short laser systems that require conversion of their original transverse intensity beam distribution.

2.7   Mode Analysis by Multiplexed HPMs

Techniques for modal characterization of complex optical fields has been developed for several applications, and particularly for fiber mode analysis [49]. It was demonstrated that holographic optical elements could provide quantized optical fields by splitting an incoming beam into a number of diffraction spots, each corresponding to a particular mode [50]. Analysis of the modal content of an incoming beam was produced by complex digital holograms displayed on a liquid-crystal-on-silicon-based phase-only spatial light modulator.

It is clear that an HPM that converts a Gaussian beam to a complex mode can also be used in reverse and produce a Gaussian beam if the same complex mode is diffracted by it. Based on this result we can conclude that an HPM could be used for modal analysis because upon illumination by a complex beam that includes the particular mode encoded already in the HPM, the resulting diffracted beam will be a Gaussian one. In addition, if several HPMs are multiplexed and have a common incident Bragg angle, then this optical element could be used to determine the multi-modal content of a beam. The concept of recording many gratings in the same volume of PTR glass has been used in the past for spectral and coherent laser beam combining [51,52]. HPMs in their nature are TBGs with encoded phase information, and therefore multiplexing of such in the same volume will give the opportunity to have simultaneously operating HPMs that diffract only specified modes.

31
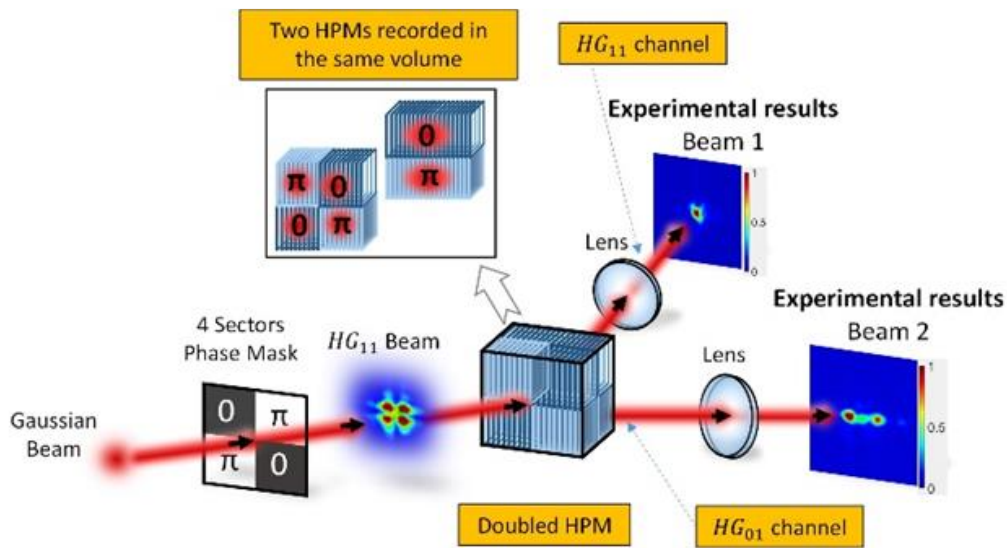
Figure 2-18 Mode analysis system utilizing multiplexed holographic phase masks.

The experimental proof-of-concept system is shown in Fig. 2-18. First, the beam in a Hermite-Gaussian mode (HG_{11} specifically) was produced from a Gaussian beam using a 4-sector conventional phase mask [20]. The HG_{11} beam then illuminated a multiplexed HPM. The multiplexed HPM was a superposition of two HPMs with encoded phase information related to the HG_{11} and HG_{01} modes, respectively. They occupied the same volume in the PTR glass plate. While the incident Bragg angles for both HPMs coincided, the diffraction angles were different. CCD cameras were placed in focal planes of the lenses to detect the far field beam profiles.

In this particular case, the images acquired by a CCD camera show that the intensity profile measured in the diffracted beam that corresponds to the HG_{11} mode (Beam 1) is Gaussian while diffracted beam that corresponds to the HG_{01} mode (Beam 2) is not, showing that only one HPM will correctly convert the mode to a Gaussian profile. Thus, by examining which diffracted beam is Gaussian one can determine the mode of the incident beam. For this experimental proof-of-concept, only two HPMs were recorded in the glass plate. However, more than 20 VBGs can be recorded in a single PTR glass plate. Using such a multiplexing approach, one single optical element could be capable of performing a simple but conclusive

32

modal analysis. Another experimental demonstration of multiplexed HPMs is shown in Fig. 2-19. In this case, two HPMs are multiplexed, one LG_{02} and one LG_{08} phase profiles are encoded into two tilted Bragg gratings diffracting and splitting the incoming beam at 5 and -5 degrees respectively.
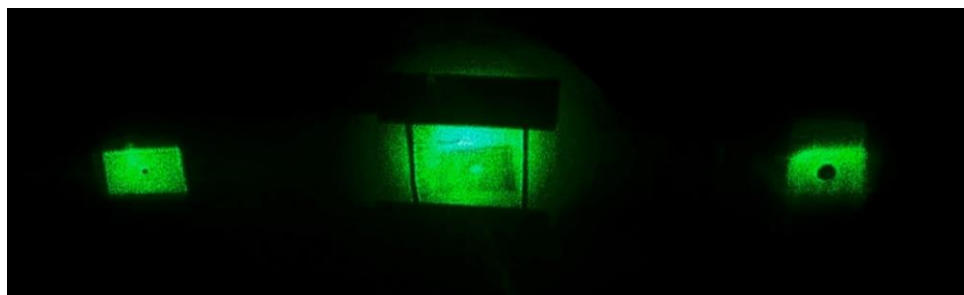
Figure 2-19 Multiplexed HPM of LG_{02} and LG_{08} at 532 nm
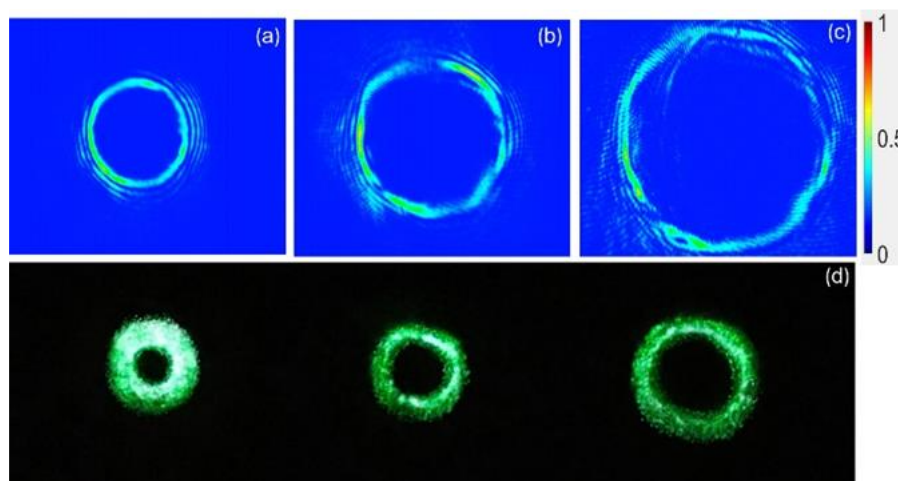
Figure 2-20 Simultaneous 3 Laguerre-Gaussian modes generation using single HPM. CCD camera images of (a) LG$_{06}$ mode; (b) LG$_{08}$ mode; (c) LG$_{10}$ mode; (d) Photograph of all 3 modes generated at the same time.

As an additional demonstration of the excellent advantage HPMs bring into the area of mode multiplexing, an HPM of a computer-generated hologram (CGH) was recorded. The CGH was designed to produce simultaneously 3 Laguerre-Gaussian modes: LG_{06}, LG_{08} and LG_{10}. Figs. 2-20 (a)-(c) shows individual images of each of the modes taken by a CCD camera, while Fig. 2-20 (d) shows a picture of all 3 modes together. We are currently working on using the same approach for mode analysis given that it will increase the capability of analyzing large number of modes while reducing the number of recorded holograms to one or few. These

results will be published elsewhere. In conclusion, the ability to record HPMs of CGHs expands substantially the application areas where HPM can be used, while simplifying and minimizing the number of holograms required.

2.8   Application of Using HPM in Intracavity Spatial Mode Conversion

A significant application of HPM is intra-cavity spatial mode conversion which is invented in our research group [53]. We provide the first work on integrating HPMs into a laser cavity for the generation of complex spatial modes. This method permits alternative phase patterns to be integrated in a laser system's outputs while keeping the intra-cavity beams' spatial structure. Due to the multiplexing potential of HPMs in PTR glass, the proposed optical system also has the unique ability to simultaneously emit various spatial modes into independent beam channels. Unlike other passive or active beam-shaping tools, the achromatic nature of these HPMs – with achievable bandwidths of several tens of nanometers and the ability to withstand up to kW levels of average power – paves the way for future developments in high-power broadband sources capable of generating light beams with arbitrary phase distributions covering any desired spectral region from near ultraviolet to near infrared.

2.9   Conclusion

Permanent HPMs recorded in PTR glass with the use of conventional SLMs show great performance and potential for mode conversion and analysis in various laser systems. HPMs provide phase transformations over a wide spectral range by angular tuning. Moreover, they can be designed to be achromatic over a wide spectral range and produce phase transformation for broadband sources such as femtosecond and high-power CW lasers. An important advantage of HPMs is the opportunity for multiplexing in the same volume of PTR glass. This

34

feature paves a way for tunable conversion to different spatial modes and for analysis of laser beams with complex mode structure, which has applications for telecom. HPMs have the potential to be integrated into a variety of optical systems, as they are passive, monolithic elements.

CHAPTER 3: REFLECTIVE HOLOGRAPHIC PHASE MASKS

3.1   Introduction

In the previous chapter we discussed transmissive-type holographic phase masks. Here we will describe the approach for making reflective holographic phase masks based upon standard RBGs. Reflective Bragg gratings (RBGs) were introduced in chapter 1, where the incoming light that matches the Bragg condition reflects back to the same side of the recording material (Fig. 3-1a). The conventional way of recording RBG is by holographically interfering two beams from one side of the sample (Fig. 3-1(a)) (called pencil geometry) and using the grating from the normal side to the recorded aperture as illustrated in Fig. 3-1(a).

The pencil geometry approach for recording RBGs possesses one main flaw if we would like to use it for recording reflective HPMs. If an RBG with encoded phase is recorded using pencil geometry, given that the readout is from the perpendicular side (Fig. 3-1a) the phase shifted Bragg gratings will be encountered by the readout beam in consecutive manner. This means that the whole beam will see the same phase change. What we are looking to achieve is that different parts of the beam encounter different phase shifted gratings. This could be done if a different recording approach is used, where the recording beams come from the opposite sides of the sample as depicted in Fig. 3-1b. In this particular case, when light is reflected from the reflective HPM, the phase dependencies will be transferred to the transverse profile of the beam. Therefore, this method provides us the ability of recording large aperture RBGs with transversely shifted parts which upon reconstruction will produce different phases to different parts of the diffracted beam. Furthermore, this way of recording allows us to record RBGs with a smaller interference angle, which was previously restricted by the limited space of the optical setup in the conventional method of pencil geometry.
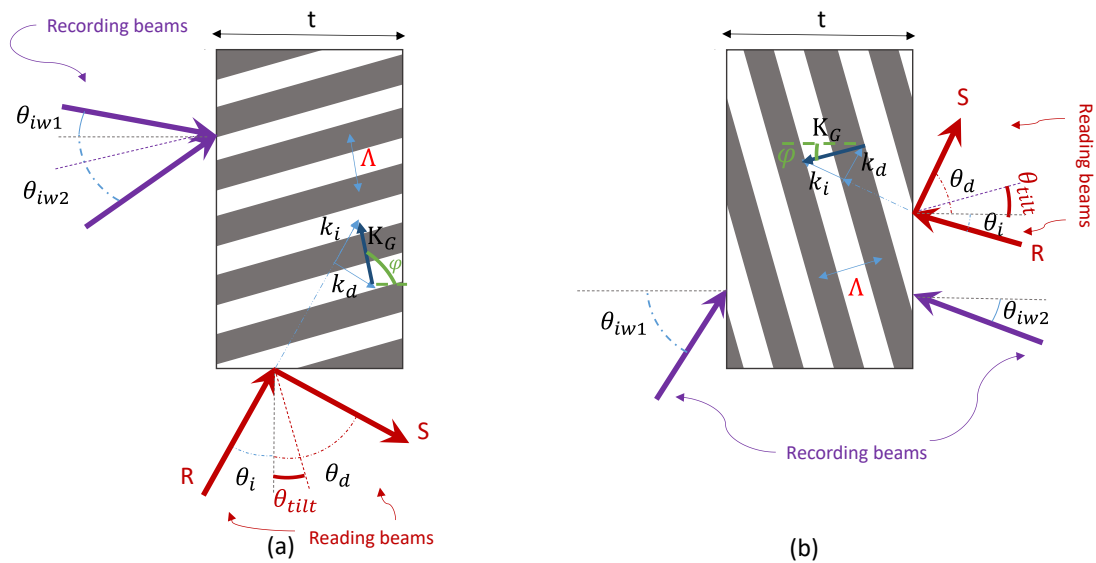
Figure 3-1 Schematic of writing and reading Bragg gratings (a) Old method of recording Reflective Bragg grating (b) Two-sided new approach of recording Reflective Bragg grating

3.2 Two-Sided Recording of Reflective Bragg Gratings Using Prisms

Using the proposed approach of recording RBGs, the sample is irradiated from two parallel sides and two beams are interfered throughout the volume of the PTR glass, two prisms are utilized to sandwich the sample, allowing two beams to refract and come from opposite sides and interfere in the volume of the sample. We can use prisms with various angles in order to refract the beams directed to the sides of the sample at the appropriate interference angle that will produce a grating with a desired Bragg wavelength.

In the holographic recording setup the angle of incidence on the prisms is determined by two UV mirrors mounted on two precise mechanical rotation stages as depicted in Fig. 3-2(a). The angle of rotation of these two mirrors must be determined to obtain the recording angle that will give as a result the grating with the desired parameters. The calculations determining the required recording angles are given below and were implemented in MATLAB (Apex. A). Fig. 3-2(b) shows the geometrical details and notations.

First, the refractive index of the glass is calculated using Sellmeier's [54] equation at recording

wavelength of 325 nm, n_{gw} , and at the reading wavelength, $n_{gr,}$.

$$n_{g\,w,r} = \sqrt{1 + \frac{0.8071 \times (\lambda_{w,r}^2)}{\lambda_{w,r}^2 - 0.0055} + \frac{0.4058 \times (\lambda_{w,r}^2)}{\lambda_{w,r}^2 - 0.0185} + \frac{0.5380 \times (\lambda_{w,r}^2)}{\lambda_{w,r}^2 - 98.0038}} \tag{3-1}$$

Where, w and r are the notations of writing and reading beams respectively. The following

relation is satisfied at the Bragg condition:

$$\cos(\theta_g - \theta_{tilt}) = \frac{\kappa_G}{2k_w} \tag{3-2}$$

where, $\kappa_G = \frac{2\pi}{\Lambda}$ is the grating vector and $k_w = \frac{2\pi n}{\lambda_w}$ is the propagation wave number of beam

inside the medium. $\theta_g = sin^{-1}(\frac{1}{n_{gr}} * \sin(\theta_{inc}))$. Therefore, the period of grating is given by:

$$\Lambda = \frac{\lambda_r}{2n_r \cos(\theta_g - \theta_{tilt})} \tag{3-3}$$

Then, knowing the period, the interference angles can be calculated propagating the rays from

the inside (the PTR glass-prism boundary) towards the air-prism interface. As it shown in the

Fig. (3.4),

$$\vec{\kappa}_G = 2\vec{k}_w \sin(\theta_w) \tag{3-4}$$

From (3-4) follows that:

$$\theta_w = sin^{-1}(\frac{\lambda_w}{2n_w \Lambda}) \tag{3-5}$$

In the case of tilted gratings, the writing angles of left and right recording beams inside the

glass can be written as:

$$\tag{3-6}$$

$$\theta_{wg-L} = \sin^{-1}\left(\frac{\lambda_w}{2n_{gw}\Lambda}\right) - \theta_{tilt}$$

$$\theta_{wg-R} = \sin^{-1}\left(\frac{\lambda_w}{2n_{gw}\Lambda}\right) + \theta_{tilt}$$

Then, the incident angles with respect to the normal to the glass inside the prisms, using Snell's

law are given by:

$$. \tag{3-7}$$

$$\theta_{wp1-L} = \sin^{-1}((n_{gw}/n_p).\sin(\frac{\pi}{2} - \theta_{wg-L}))$$

38

$$\theta_{wp1-R} = -\sin^{-1}((n_{gw}/n_p).\sin(\frac{\pi}{2} - \theta_{wg-R}))$$

where, n_p is the refractive index of the prism. Therefore, the incident angles on the prisms in air are calculated using following equations:

(3-8)

$$\theta_{wi-L} = \sin^{-1}(n_p.\sin(\theta_{wp1-L} - \alpha))$$

$$\theta_{wi-R} = \sin^{-1}(n_p.\sin(\theta_{wp1-R} - \alpha))$$

Where α is the prism angle shown in the Fig. 3-2(b). The calculated angles above are the incident angles on the prisms with respect to the normal to the prism side. Finally, the rotation angle of the mirror stages can be calculated. The reference for these mirrors is the position at which each incoming beam is reflected directly to the other mirror. Therefore, we have:

(3-9)

$$\theta_{stage-L} = (\theta_{wi-L} + \alpha)/2$$

$$\theta_{stage-R} = (\theta_{wi-R} - \alpha)/2$$

As a result, for a given Bragg wavelength and desired grating tilt we are able to determine the required recording angles.
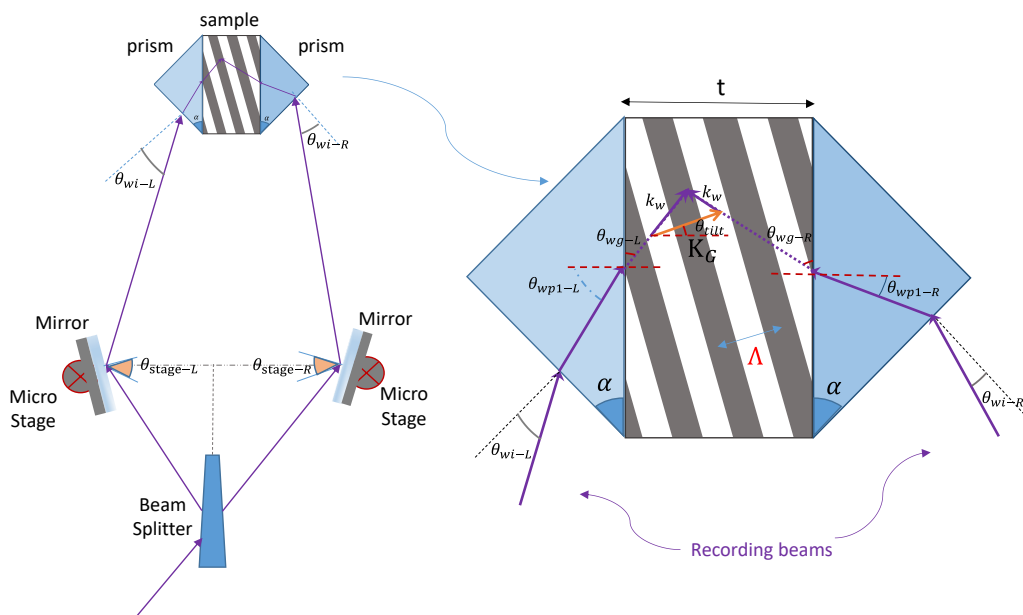
Figure 3-2 Recording RBG geometry using prisms for two sided sample exposure

We used three different prisms with different angles of α (shown in Fig. 3-2), including equilateral prism with $\alpha = 60^o$, right angle prism with $\alpha = 45^o$ and cube shaped prism with $\alpha = 90^o$. In order to record RBG at short wavelengths such as visible wavelengths we determined that the use of equilateral and right angle prisms is most suitable, while for longer wavelengths like above 800 nm the proper prism is the cube one with $\alpha = 90^o$. For example, to record an RBG performing at 1030 nm with 0° incident angle, we used two fused silica cubes to sandwich the sample in between, and set the rotation angle of the mirrors to the calculated values of $\theta_{stage-L} = 36.98^o$ and $\theta_{stage-L} = -36.98^o$. The sample dimensions were $25mm \times 25mm \times 1mm$ and as a result an RBG with aperture of $25mm \times 25mm$ was recorded. Its diffraction efficiency was more than 90% and the central wavelength was only 50 pm above 1030 nm.

3.3   Reflective Holographic Phase Mask (RHPM)

By recording transversely shifted phase profiles inside an RBG, a reflective holographic phase masks (reflective HPM) was invented by our research group. To achieve that, a master phase mask placed between the prism and the sample was used. Using this technique for encoding the phase into the RBG, a 4-sector (HG_{11}) reflective holographic phase ask (shown in Fig. 3-3) was recorded. To make the system more flexible, we implemented an SLM device for encoding the phase pattern in the signal beam instead of the phase mask approach (Fig. 3-4). Results from that approach will be published elsewhere.
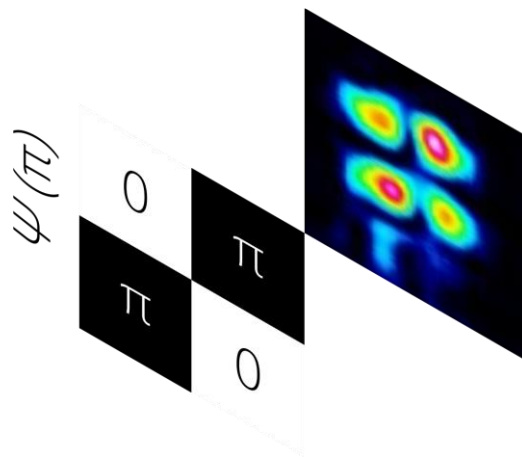
Figure 3-3 Reflective Hologrphic Phase Mask of HG_{11} mode
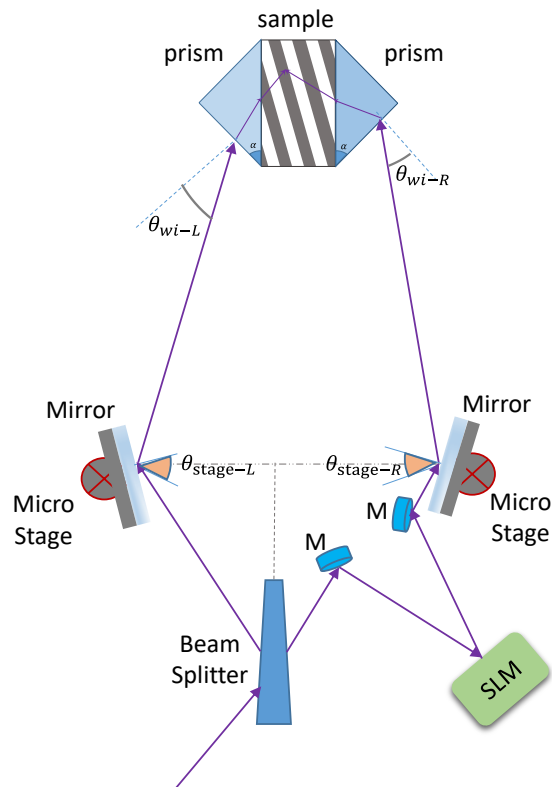
Figure 3-4 Schematic setup of recording reflective holographic phase mask

CHAPTER 4: TWO-DIMENSIONAL TRANSMISSIVE HOLOGRAPHIC BEAM SPILITTERS FOR AUGMENTED REALITY APPLICATIIONS

4.1 Introduction

Head-up displays (HUDs) are used in transportation vehicles to reduce the amount of time the driver spends looking away from the road. Traditional head-up-displays suffer from a limited field of view and a lack of compactness mainly due to the use of bulky optics (i.e., projection optics, folding mirrors, and beam combining optics) (Fig. 4-1(a)). To increase the size of the perceived image and field of view, the size of this optical elements must be increased. Because most vehicles have a limited amount of space, expanding the size of optical elements becomes an impractical approach. Another problem is the narrow window/position called also the "eye-box", within which the viewer can see the entire projected image (illustrated in Fig. 4-1(b)). If the observer moves her or his head out of the eye-box, the image begins to be clipped by the edge of the window. Greater head movements eventually cause the image to vanish completely.
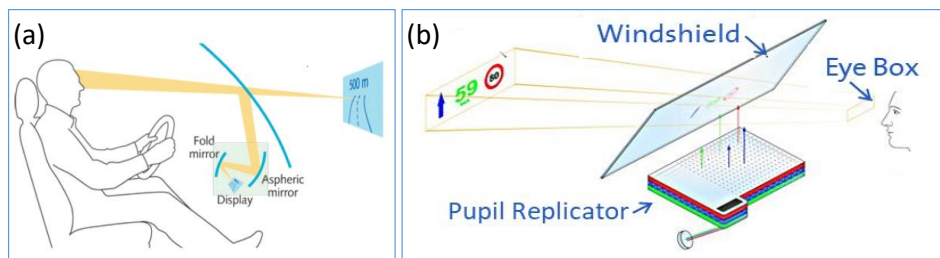
Figure 4-1 (a) Traditional HUD with mirrors (b) HUD with expanded eye-box with flat optics

Recent research has explored the use of holographic optical elements (HOEs) in the development of head-up displays with the purpose of expanding the eye-box and making the projection unit as a whole, lighter, and more compact. HOEs are typically recorded in

photosensitive polymers [1] and being organic materials, photopolymers are sensitive to the environmental conditions which affects their reliability and as a whole their lifetime. The aim of the research presented here is to develop a 2D diffractive beam splitters for enlarging the exit pupil of HUDs. The splitting elements are recorded in PTR glass which guarantees robustness and very little sensitivity to environmental conditions.

4.2   Augmented Reality (AR) Head-Up Displays

An augmented reality head-up display includes an image generation (display) unit, magnifying optics and a combiner to overlay the display content and physical world (Fig. 4-2). AR devices can be classified into partial-mirror and grating-based setups based on the type of combiners used that are shown in Fig. 4-2 [55].
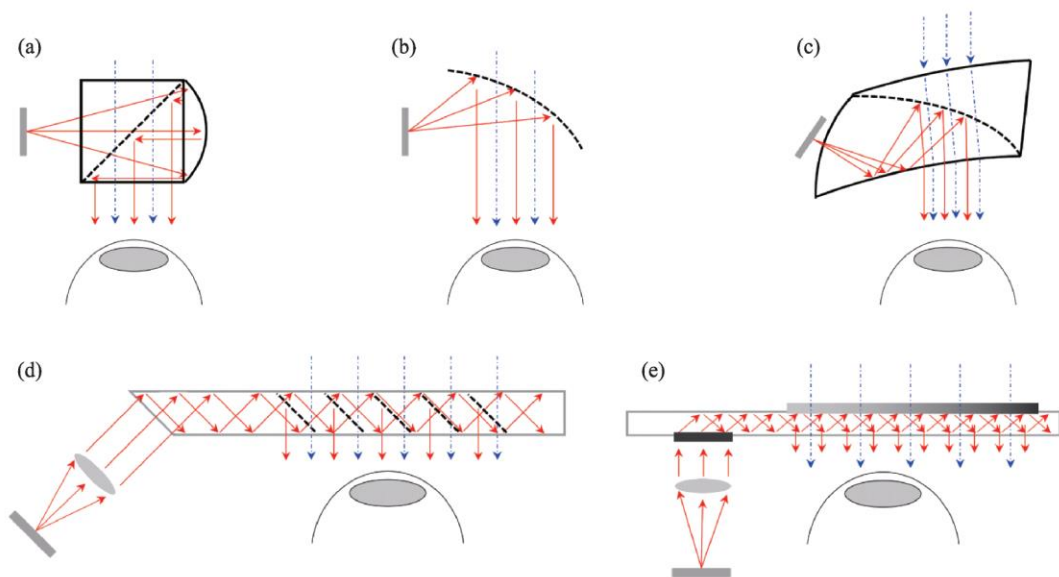
Figure 4-2 Augmented reality configurations. (a-d) partial mirror based (e) grating based AR 55

The Google Glass optical design, which uses a beam splitter cube as the combiner shown in Fig. 4-2(a), is a typical example of partial-mirror based AR devices [56]. A reflective concave mirror directly on the beam-splitter cube operates as the magnifying optics. Fig. 4-2(b) depicts a different configuration that uses a free-form partial reflector [57,58] as both a

magnifying optics and a combiner, effectively eliminating the need for additional magnifying optics (e.g., Mira, Meta 2, and DreamGlass). NED AR uses a free-form prism performs as the magnifier and combiner shown in Fig. 4-2(c) [59,60]. This configuration provides smaller size with decent image quality and FOV. To further reduce the size a partial reflector array (e.g., Lumus [61,62]) could be used because the thickness of the combiner optics can be reduced even more in this configuration. Because of the waveguide's narrow angular range, this design sacrifices FOV. In parallel, multiple reflections are possible and could result in stray light and non-uniform intensity, which would reduce the image quality. As a whole, the optical quality and efficiency of partial-reflector based AR are higher, except for the partial mirror array configuration.

Grating-based waveguide AR devices use diffraction to direct display light via a thin glass plate (the "waveguide") with a thickness ranging from 0.3mm to 1mm. In general, an input-coupling grating is used at the display end to diffract input light to an angle greater than the critical angle, as shown in Figure 4-2(e). Through total internal reflection (TIR), the diffracted light will then flow toward the viewing region. In front of the eye, an output-coupling grating is used to diffract TIR-guided light so that it goes toward the observer.

Low-efficiency gratings with gradient efficiency are commonly used to distribute light over a broader eye box; the process of spreading light across a wide eye box is known as exit-pupil expansion or pupil replication. The dispersive nature of gratings, as well as various diffractions, make establishing a large FOV and uniform output intensity difficult. When a white image is shown, this emerges as visible color non-uniformity across the FOV. In order to obtain greater homogeneity, total efficiency is frequently sacrificed. Despite the lower display quality, the desire for a smaller form factor keeps grating-based waveguide AR devices in the spotlight.

4.3 Review of AR Head-Up-Display Eye-Box Expansion Methods

The product of the area through which light flows and the light's spreading angle is conserved in an optical system, which is known as étendue or Lagrange invariant [63]. The size and pixel pitch of the image generation display unit (e.g. SLM) determine the holographic display's etendue. As a result, the size of the intrinsic exit-pupil E is determined as follows [64]:

$$E = \frac{L\lambda}{2p\sin(FOV/2)} \qquad \text{4-1)}$$

where, L is the display's size, p is the display's pixel pitch, and λ is the light source's wavelength. The size is slightly more or less than two millimeters for the bandwidth of 2k or 4k SLMs now available on the market to deliver 45° of FOV. As a result, the holographic near-eye display's exit pupil must be very small in order to provide a sufficient FOV. A holographic near-eye display that satisfies both large FOV and large eye-box size has not been introduced. There are ways for expanding the eye-box size by modifying the trade-off relation of étendue. For example, See-real has created a system that alters the viewing window of a large-scale flat panel-type holographic display by using a directional backlight and eye-tracking technology [65]. Other 3D displays, such as compressive light field or depth fused displays, have investigated similar methodologies [66].

In near eye displays, a famous approach to increase the FOV with a large two-dimensional (2D) exit pupil (optimized etendue), is to replicate the exit pupil. Various methods of 2D exit pupil replication have been developed from waveguide-based image replicator to grating-based waveguide devices and reflective surface image replicator. The image replicator is configured for receiving a beam and image the source to a number of replicated images. Therefore, at any position of the viewer's eye at least one beam (image) impinges onto the eye's pupil. The image replication results in expanding the eye-box of the display while preserving the wide Field-of-View (FOV). The original patent to use exit pupil replication

method was authored by Jean-Blaise Migozzi [67] in 1990 and demonstrated the design of an optical device that enables an observer to look simultaneously at what is normally in his field of vision and at collimated image.

Fig. 4-3(a) shows a waveguide-based image replication. In operation, each beam received from the first waveguide is split into a plurality of beams that form a 2D array of beams of image light, as shown in Fig. 4-3(b). The combiner, relay and refocus 2D beams parallel to each other at the eye-box.
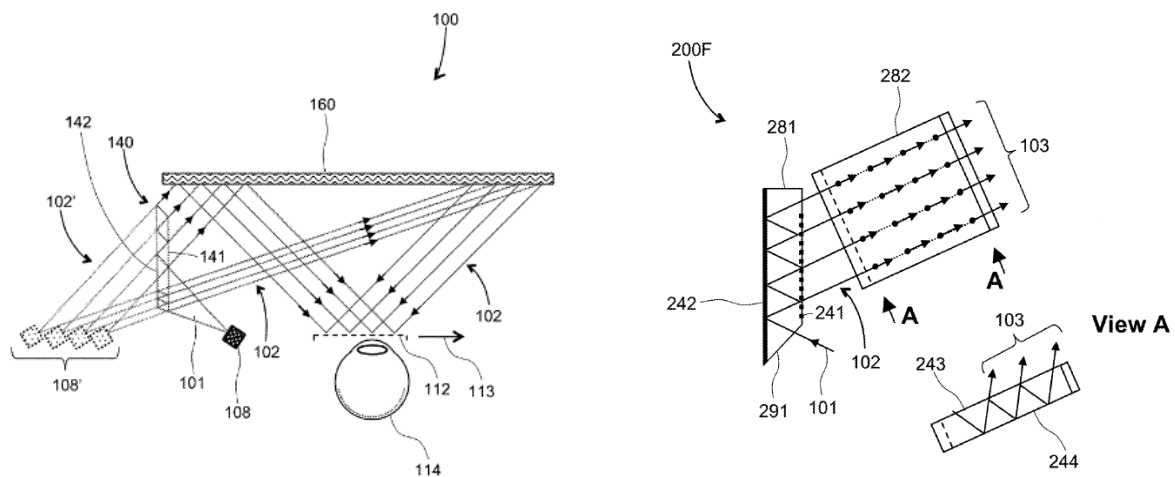
Figure 4-3 (a) 140 image replicator, 160 combiner, 141 translucent reflective surface, 142 blind reflective surface, 108 projector, 101 diverging first beam, 102 plurality of second beams, 108' plurality of virtual projectors, emitting virtual second beams, 112 eye-box, 113 second beams converging and laterally offset, 114 user's eye (b) 281 first waveguide, 282 second waveguide, 243 third surface, 244 forth surface, 103 2D array of light [68]

Figure 4-4 shows the grating-based waveguide image replicator architecture used in Magic Leap headset (2018) [69]. The in-coupling and out-coupling diffraction gratings are arranged on the two sides of the waveguide plate. The in-coupling diffraction grating is set up to modify the beam's ray angles, causing light to flow in a zigzag pattern through the waveguide via total internal reflection (TIR). The output coupling grating is designed to change the ray angles of the beam so that light no longer propagates through TIR and exits the waveguide. The out-coupling grating may have a low diffraction efficiency to allow the formation of numerous beams, and the diffraction efficiency may be changed spatially to improve output 2D beam

homogeneity. Any diffractive (blazed, slanted, binary and etc), holographic, polarization-based, or resonant structure, such as a surface relief grating (SRG) or volume reflective holograms in photopolymers, can be used as a diffraction grating.
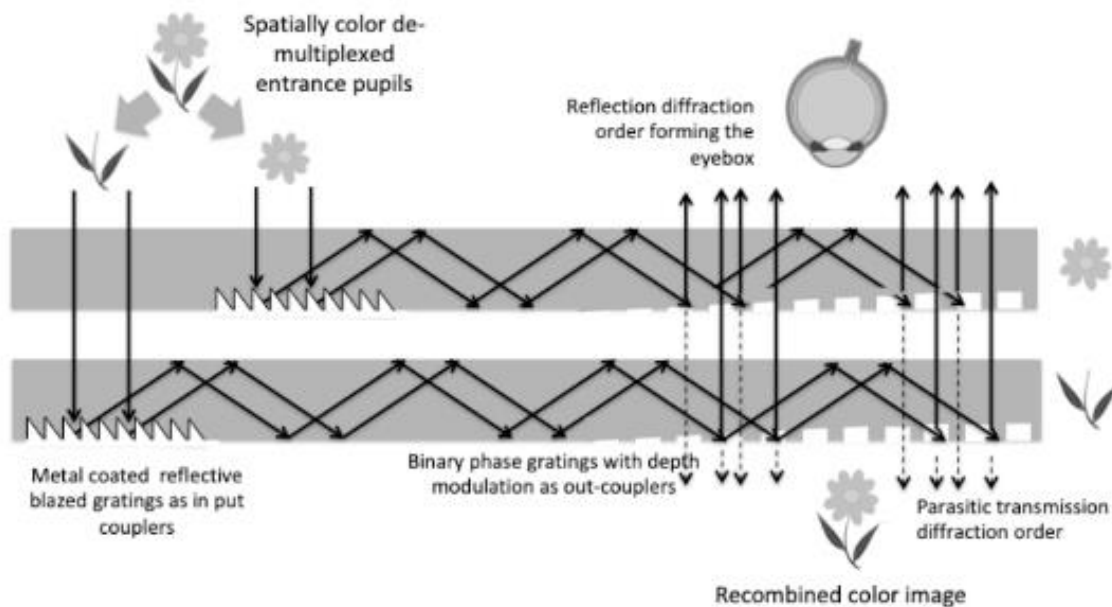
Figure 4-4 Spatially color-de-multiplexed input pupils with100% reflective blazed gratings as in-couplers and binary phase gratings as out-couplers (Magic Leap) [69]

Recently transparent volume holograms working in reflection mode recorded in photopolymers such as Bayfol by Covestro/Bayer (Germany), photopolymers by Dupont (US), Polygrama (Brasil) or Dai Nippon (Japan), have been used to implement in- and out-couplers in waveguide combiners. They can be made to perform at a single wavelength or across the full visible spectrum. Figure 4-5 shows both thin and thick volume holograms operating in reflection and transmission modes. The top part of the figure shows a typical 1D exit pupil expander with a single transmission volume hologram sandwiched in between two plates. When the field transverses the hologram downwards, it is in an off-Bragg condition, and when it transverses the volume hologram upwards after a TIR reflection, it is in an on-Bragg condition, or close to it, therefore creating a weak (or strong) diffracted beams which break the TIR condition. Even though the approach gives good results, such hologram sandwiched in between plates is complex to produce [69].

47
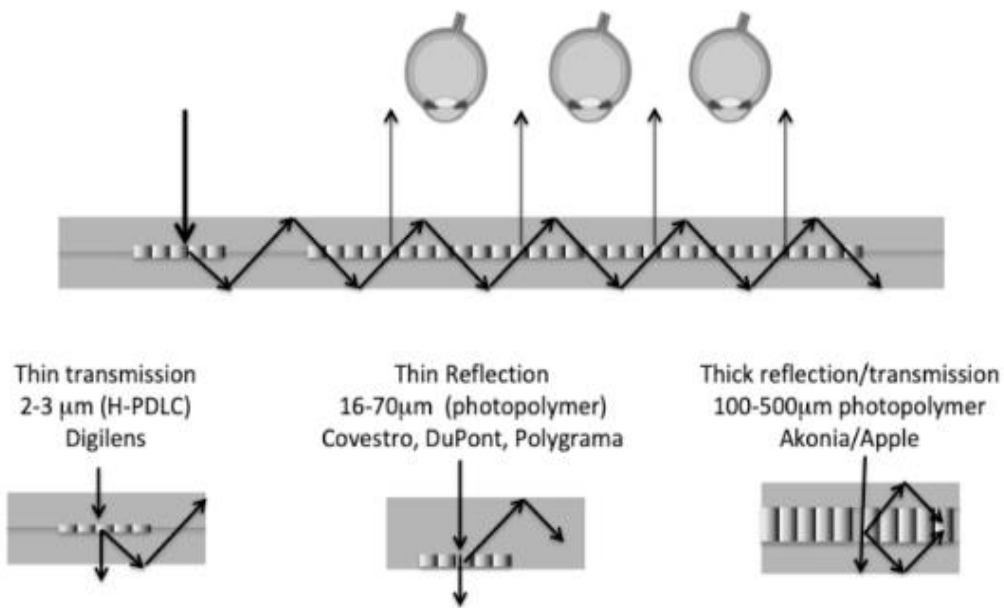
Figure 4-5 Different types of photopolymer volume holograms acting as in and out couplers in waveguide combiners [69]

There is also mirror-based image replicator, where a deformable mirror is utilized to improve the FOV and the eye-box of an HUD incorporating system. The illustrated schematic of the system is shown in Fig. 4-6 and includes light source 205, deformable mirror 210, actuator system 215 and partially transparent combiner mirror 220.
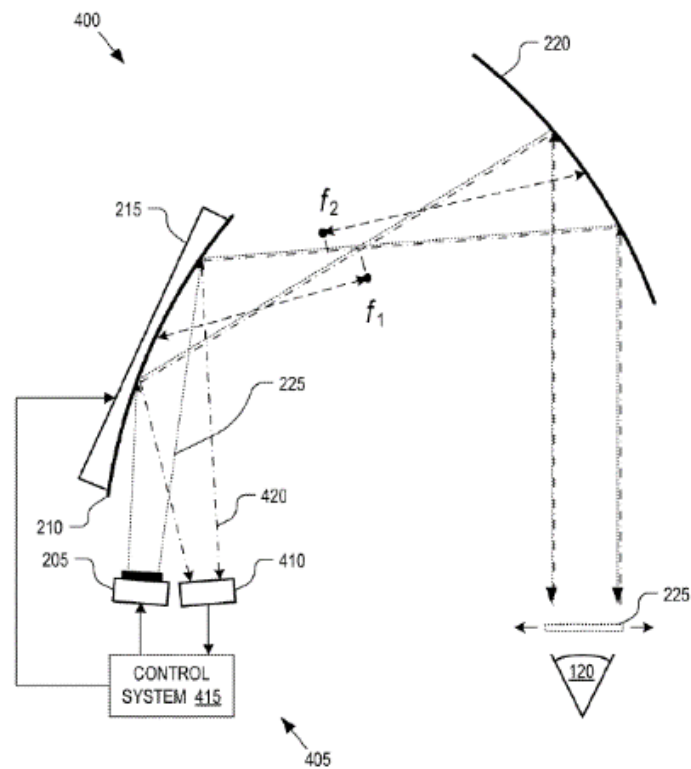
Figure 4-6 Mirror-based image replicator in head-up-display for FOV and eye-box expansion [70]

In conclusion, holographic optical elements find broad application in the development of head-up-displays with the goal of enlarging the eye-box and making the projection unit as a whole lighter and more compact. HOEs are typically recorded in photosensitive polymers [1] and because photopolymers are organic materials, they are sensitive to the environmental conditions, affecting their reliability and overall lifetime. The aim of the research presented in the next chapter is to develop a 2D volume diffractive beam splitters capable of enlarging the exit pupil of HUDs. These splitting elements are recorded in PTR glass, which ensures robustness and low sensitivity to environmental conditions. The theory and the experimental results of this 2D diffractive beam splitters are presented in the following.

4.4   Theory of Raman-Nath Diffraction Beam Splitters

Light diffraction can be produced by periodic phase gratings that operate in two regimes. First one is the Bragg regime[71], which produces a single diffracted wave when the Bragg condition is satisfied. Gratings operating at this regime are known as volume Bragg gratings (VBGs) [19]. Second regime is the Raman-Nath regime [72], which produces many diffracted beams. Due to this, the Raman-Nath regime is suitable for producing beam splitting and is implemented by surface or thin volume gratings. However, our theoretical and experimental studies described in this chapter revealed that thick volume gratings can operate in Raman-Nath regime and produce higher harmonics, achieving similar to the results produced by surface relief gratings. In this project, we recorded such volume gratings in PTR glass and were able to produce two-dimensional (2D) beam splitting of laser beams and images.

The theory of periodic phase gratings has been extensively studied [21,73-75]. Periodic phase structures operate in two different regimes, as we previously mentioned. The first one is Bragg regime, which produces only one diffracted wave when the incoming wave is at the Bragg incidence angle. Second, is the Raman-Nath regime, in which several beams are diffracted by the grating. In order to distinguish between the two diffraction regimes, Klein and Cook [74] introduced a Q parameter, which is defined as $Q = 2\pi\lambda_0 d/\Lambda^2 n_0$ (where, λ_0 is the vacuum wavelength of light, d is the grating thickness, Λ is the grating period and n_0 is the mean refractive index). Thin gratings are assumed to have values of $Q < 1$, while thick gratings operating in the Bragg regime have values of $Q > 10$. The validity of the parameter Q as a tool for predicting the diffraction regime though has been questioned by a number of theoretical arguments and experimental observations. Moharam et. al. [76-79] introduced a different parameter called $'\rho'$ that more accurately determines whether a grating operates in the Raman-Nath or Bragg regimes:

$$\rho = {\lambda_0}^2/\Lambda^2 n_0 \delta n \qquad (4\text{-}2)$$

where, δn is the refractive index modulation and the rest of the parameters are similarly defined as for Q. The important difference between the two parameters is that ρ does not depend on the thickness of the grating (Eq. 4-1). Therefore, for large grating periods Λ and high index modulation δn (and disregarding the thickness of the grating) higher order diffracted beams become present even for thick gratings. As a consequence, when $\rho \gg 1$ the incident beam is only transferred into one diffraction order (Bragg regime), and when $\rho \le 1$ the incident beam is transferred to multiple orders which corresponds to the Raman-Nath regime.

As shown in Eq. 4-1, producing several diffracted beams is related to increasing the period of grating and achieving high refractive index modulation. To simulate diffraction of light in volume gratings operating in Raman-Nath regime, we employed numerical rigorous-coupled-wave-analysis implemented in MATLAB (Appendix. B). For the purpose, the incoming light field is diffracted by a periodic phase structure described as spatially periodic permittivity. The light field is represented by a scalar wave equation,

$$\nabla^2 E - k^2 E = 0, \qquad (4\text{-}3)$$

where, $k^2 = \beta^2 - j\alpha\beta$, $\beta = 2\pi n_0/\lambda_0$ is the propagation constant of the electro-magnetic field, n_0 is the material's refractive index and α is its absorption coefficient. A binary modulation of the refractive index was assumed, and the periodic permittivity was expanded into Fourier series. The electric field was represented by its Fourier expansion as

$$E = \sum_{l=-\infty}^{\infty} \phi_l(z)\, exp(-j\bar{\sigma}_l.\vec{r}), \qquad (4\text{-}4)$$

where, $\bar{\sigma}_l = \bar{\sigma}_0 - l\overline{K}$, $\overline{K}$ is the grating vector, l is the order of diffraction mode, and $K = 2\pi/\Lambda$, $\bar{\sigma}_0$ is the wave vector of the incident wave ($l = 0$) and $\vec{r} = (x, y, z)$. Substituting the field and the refractive index modulation into the scalar wave equation and neglecting the second derivative with respect to z, we obtain the well-known coupled wave equations [76]:

$$\frac{\partial \phi_l}{\partial \xi} = j\rho l^2(1 - B_l)\phi_l + j(\phi_{l-1} + \phi_{l+1}) \qquad (4\text{-}5)$$

where, $B_l = 2\Lambda\sin\theta_0/\lambda_0 l$, θ_0 is the external angle of incidence, $\xi = v\left(\frac{z}{d}\right), v = \pi\delta nd/$ $\lambda_0\cos\theta_1$, θ_1 is the angle of diffraction of the zeroth-order mode and d is the grating thickness. Effective energy transfer to higher order modes requires the factor ρ to become less than 1, which corresponds to Raman-Nath diffraction mechanism. Solving the set of equations 3-4 in MATLAB by tangential field matching at the interface between the input and the grating regions, provides the intensity of lth mode by $\phi_l^*(v)\phi_l(v)$. In the simulation results, we see that by designing the grating in such a way that the parameter ρ becomes less than 1, energy starts to transfer to higher order modes. This is the characteristic behavior that is needed in order to produce beam splitting holographic optical element.

For an un-slanted transmission grating, the results for the diffraction efficiency as a function of d/Λ are displayed in Fig. 4-7. The period of the grating is designed to be $\Lambda = 28$ μm which at the wavelength of 532 nm corresponds to 1.09 degrees separation angle between the diffracted beams. The grating thickness is chosen to be 2.2 mm in order to produce uniform intensity distribution among the first 5 modes (0, ±1 and ±2).
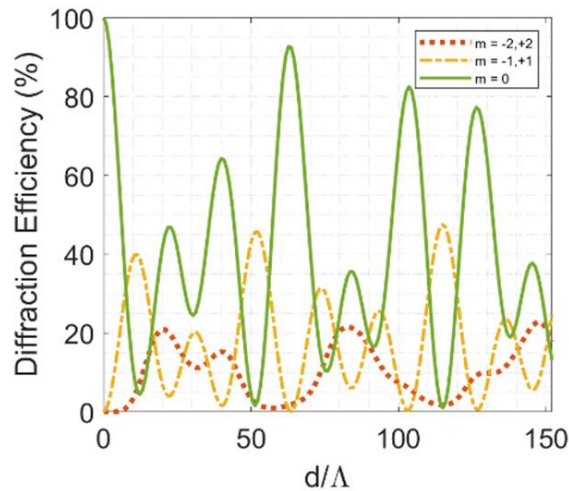
Figure 4-7 The diffraction efficiencies of $0, \pm 1, \pm 2$ diffracted beams for transmission grating with $\rho < 1$.

Variation of the diffraction efficiency for different orders as a function of the incident angle to the grating is depicted in Fig. 4-8. Unlike the Bragg regime, where the incident beam is diffracted at a fixed angle at one diffraction order [80], here there are several higher orders that occurs at numerous incident angles. In addition, there are higher diffraction orders that fluctuate by varying the incident angle. We see that at zero incident angle, the diffraction efficiency of the first 5 diffraction orders is identical. Therefore, the incident beam is diffracted to 5 uniform beams and performs as a 1D equal intensity beam splitter.
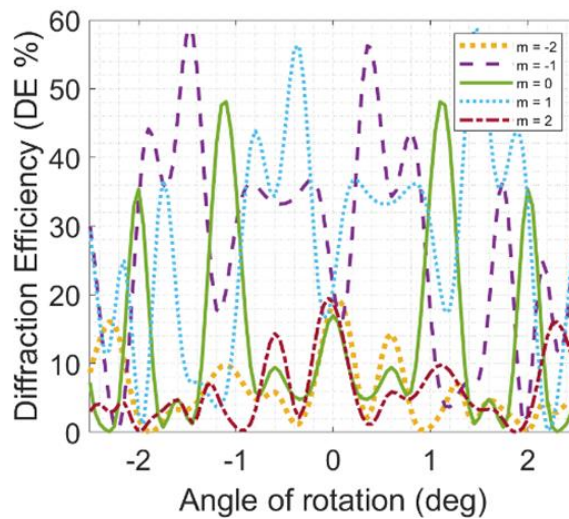
Figure 4-8 Angular dependence of diffraction efficiency of higher orders at Raman-Nath diffraction regime with $\rho < 1$

In a different perspective, Fig. 4-9 depicts the diffraction efficiency of the higher order modes at zero incident angle. It clearly shows that using particular values for thickness, period, wavelength, and index modulation, can provide five diffracted beams with equal intensity.
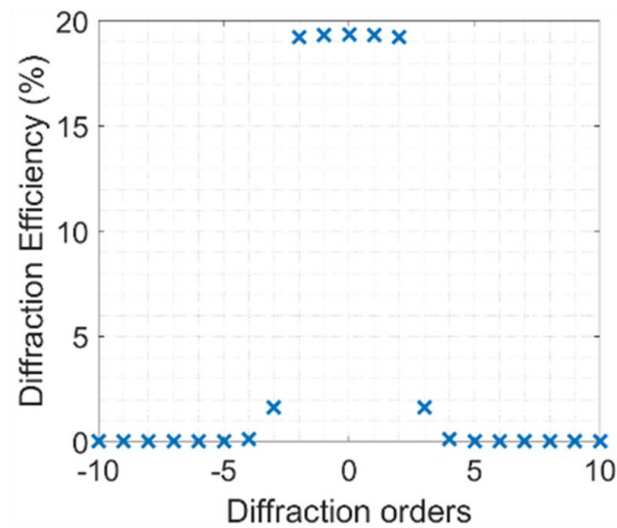
Figure 4-9 Producing a beam splitter using a Transmissive grating in the Raman-Nath regime

4.5 Development Of Raman-Nath Diffraction Beam Splitters

By applying the calculated period and index modulation   transmissive gratings were recorded in the volume of PTR glass. The gratings were designed to provide 4 or 5 diffracted orders with uniform efficiency. Figs. 4-10(a and b) shows the performance of the recorded beam splitting gratings applied in horizontal and vertical directions and operating at 532 nm. The X-direction beam splitter was recorded in a 2.2 mm thick PTR glass having $28 \ \mu m$ period which produced 1.09^o angle of separation between the diffracted beams at 532 nm. The required index modulation of the grating was minimum 250 ppm in order to operate in the Raman-Nath regime. The experimental result in Fig. 4-10(a) illustrates five diffracted beams with identical intensities and four higher order beams with low efficiency, which is consistent with the calculations presented in the preceding section. The same approach was used to holographically record the Y-direction beam splitting grating that diffracted beams at an angle of separation 0.68^o (Fig. 4-10(b)). RCWA calculations showed that in order to improve the homogeneity of the diffracted beams, the thickness of the grating in this particular case should be 3 mm. However, for simplicity, in the provided experimental results the vertical grating was

also recorded in a 2.2 mm PTR glass. Therefore, the homogeneity of the diffracted beams was not as optimized as much as for the X-direction grating, but as a whole the uniformity was improved by recording grating with higher index modulation, as it is illustrated in the experimental results of Fig. 4-10(b). The two recorded gratings were then combined to form a two-dimensional beam splitting device. Figure 4-10(c) shows the 2-dimnesional beam splitting results at 532 nm.

The same development process was used to create two gratings that operate at 633 nm. These gratings were designed to have the same angle of separation between the diffracted beams as for the one operating at 532 nm. As a result, the gratings were recorded with periods of 33.2 μm and 52 μm, to operate with separation angles of 1.09^o and 0.68^o, in horizontal and vertical directions respectively. Figure 4-11(b) shows the two-dimensional spot array generated by the two gratings. In the presented experimental results, the gratings were recorded in PTR glass with the same thickness of 2.2 mm, as for the green beam splitters. However, in order to improve the uniformity of the diffracted beams, the required thickness of the glass has to be 2.7 mm and 3.55 mm for the horizontal and vertical directions respectively and the index modulation needs to be more than 800 ppm.
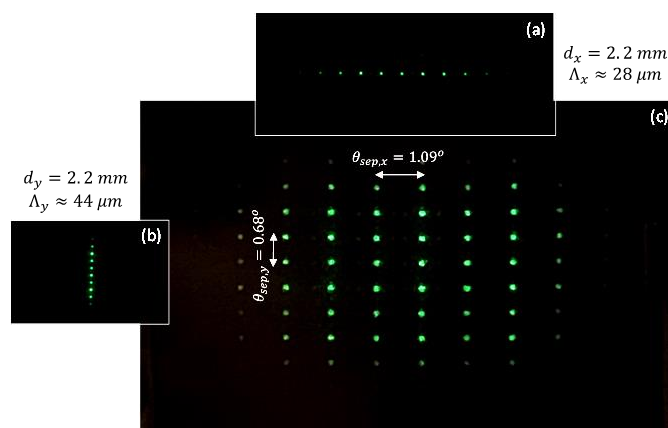
Figure 4-10 Experimental results of 1-D horizontal and vertical array of beams are presented in a,b respectively and 2-D array of beams represented in c at 532 nm.
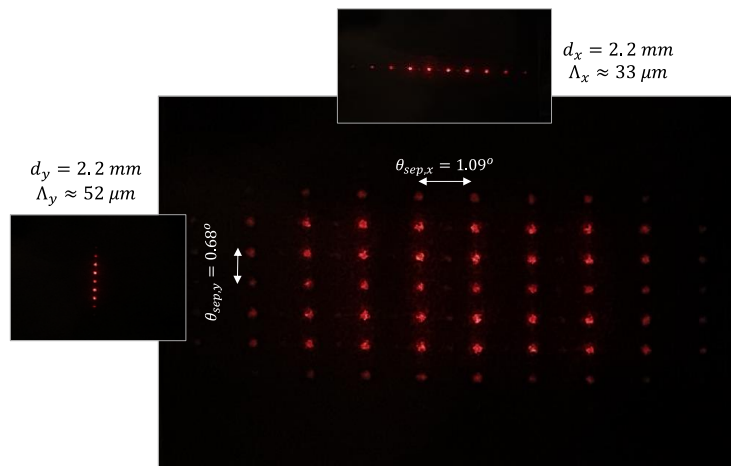
Figure 4-11 Experimental results of 1-D horizontal and vertical array of beams are presented in a,b respectively and 2-D array of beams represented in c at 633 nm.

4.6   2-D Transmissive Holographic Beam Splitters for Head-Up-Display Eye-Box

Expansion

For performance evaluation of the developed 2D Raman-Nath beam splitters for image multiplication, a spatial light modulator (SLM) was used to generate images. An expanded laser beam was reflected by the SLM, encoding a computer-generated hologram of the desired image. For setup alignment purposes, a pattern including horizontal and vertical lines with different thicknesses was chosen. The SLM phase pattern was projected in far-field by a lens and as a result an array of images was constructed. The whole setup used for image multiplication is illustrated in Fig. 4-12.
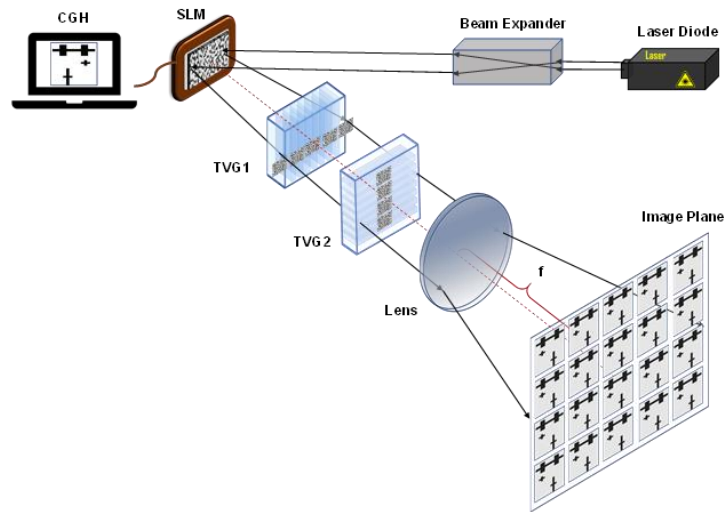
Figure 4-12 Schematic of experiments to test image multiplication using beam splitter transmissive gratings. TVG: Transmissive Volume Grating; CGH: Computer-Generated-Hologram; SLM: Spatial Light Modulator

4.7   Spectral Beam and Image Combination

Figures 4-13 and 4-14 show that images can be successfully replicated using the proposed and designed 2D Raman-Nath beam splitters at wavelengths of 532 nm and 633 nm, respectively.

Figure 4-13 Image multiplication result at 532 nm
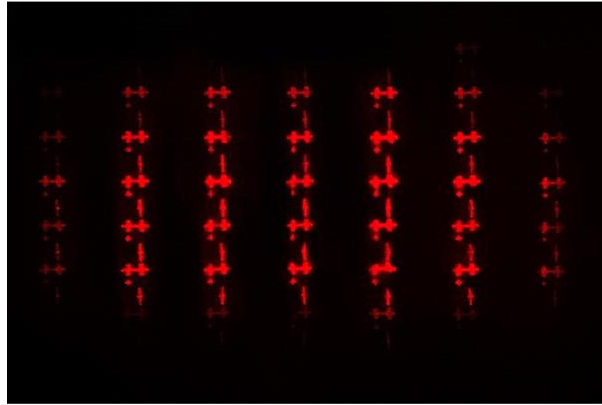
Figure 4-14 Image multiplication at 632 nm

The final result being white light images, we implemented the beam combining setup depicted in Fig. 4-15. Two spatial light modulators (as image generation units) were to generate the holograms of the desired images. The SLM generated phase patterns were transmitted through the Raman-Nath beam splitters which were arranged for each particular color next to each other with no gap in between. A short-pass dichroic mirror (Thorlabs, DMSP605nm) with a proper angular acceptance was used for spectral beam combining by transmitting the green and reflecting the red beams. An array of images was reconstructed at the focal length of a lens (f=1m). The resulting red and green image combination is illustrated in Fig. 4-16. There are several flaws in the resulting image such as not a uniform color combining and sharpness of the pattern. The sharpness is due to the fact that two different SLMs with different resolutions were used for the simultaneous image generation (one with 10um and one with 8 um pixels).

The second problem illustrated in the image is the non-uniform intensity and the lower number of replicated red images which is related to the properties of the recorded splitting gratings. This issue can be solved by recording the gratings with the exact parameters including thickness and index modulation values.
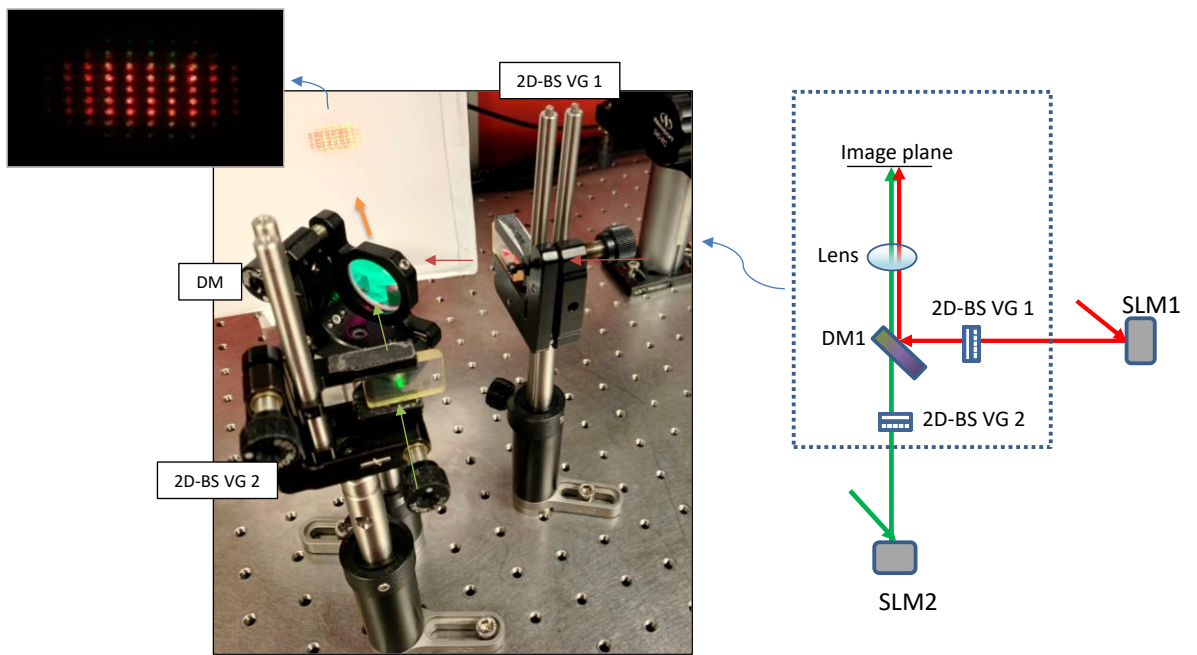
Figure 4-15 Image combining setup
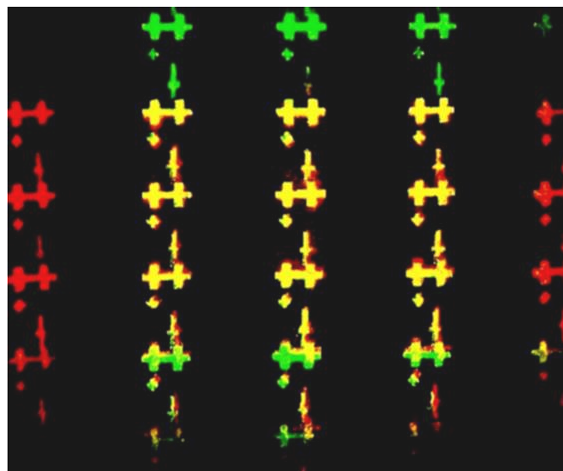
Figure 4-16 Image combination at wavelengths of 532 nm and 633 nm

In summary, we holographically recorded transmissive gratings in the volume of photo-thermo-refractive glass by applying the parameters of period and index modulation so the gratings performed in Raman-Nath regime. The diffracted higher orders had uniform diffraction efficiencies and were successfully used to generate an array of images. The results therefore show that this approach can be successfully used for enlarging the exit pupil of augmented reality systems.

CHAPTER 5: SUMMARY AND CONCLUSION

The transmissive holographic phase mask, which is a transmissive Bragg grating encoded with a phase profile of interest, is developed in this thesis. A holographic recording system based on a standard Mach-Zehnder interferometer was employed. Interfering the signal and reference UV beams of an interferometer creates a phase pattern that is applied to a volume of PTR glass which cause a permanent change in local refractive index caused by further heat development process. To make an HPM, a master phase plate or SLM with the suitable phase distribution is inserted into one of the interferometric arms. The spatial profile of the signal beam's phase element is transferred to the photosensitive recording media, where it is superimposed on the plane phase-front of a periodic pattern formed by the interference of the signal and reference beams.

In addition, we started the development of a new holographic optical element called reflective holographic phase mask. The holographic recording setup was developed accordingly so we can record RBGs with transversely shifted sections across the aperture, resulting in different phases for various regions of the Bragg diffracted beam. RBG's diffraction spectrum possesses a very narrow bandwidth, and the holographic recording technique allows to multiplex multiple gratings into a single volume of PTR glass. If each of these Bragg wavelengths is assigned with a specific spatial mode, simultaneous spatial and spectral multiplexing could be achieved. Additionally, this approach of recording allows us to record RBGs applying smaller interference angles, which was not the case for the pencil recording geometry.

Finally, we used the parameters of period and index modulation of holographically recorded transmissive gratings to generate several diffracted beams by designing them to perform in Raman-Nath regime. The Raman-Nath gratings were designed to have higher order

diffracted beams with uniform diffraction efficiency and were successfully employed to create an array of images. This method can be used to increase the size of the exit pupil in augmented reality systems.

Future works include improving the recording setup for a reflective-type HPM. Furthermore, angular and spectral multiplexing multiple gratings into both single TBG and RBG that each Bragg grating to be assigned with a specific spatial mode to achieve simultaneous spatial and spectral multiplexing and demultiplexing in both transmissive and reflective type HPMs.

APPENDIX A: MATLAB CODE FOR RBG DOUBLE-SIDE

RECORDING USING PRISMS

```
%% Recording RBG from both sides using prisms
% Nafiseh Mohammadian 2020

%% inputs
% lambda_r     Reading wavelength [nm]
% theta_Inc     The incident angle in the air [deg]
% theta_tilt    The tilt angle of gratings inside the glass [deg]
% t             The thickness of the glass [mm]
% DE            The desired diffraction efficiency [percentage]
% Apx           The apex angle of the prism [deg]
% alpha         The side angle of the prism [deg]

%% Outputs
% period=per          The grating period of an RBG [um]
% TwL=theta_iL        Angle of incident of left recording beam on the prism [deg]
% TwR=theta_iR        Angle of incident of right recording beam of on the prism
[deg]
% TStgL=theta_StgL    The angle of the left stage    [deg]
% TStgR=theta_StgR    The angle of the right stage   [deg]
% dn=delta_n          The index of modulation to get the targeted DE [ppm]
%%
function []=RBG_prism_NaMo(lambda_r,theta_Inc,theta_tilt,t,DE,alpha)

  lambda_w=0.325;  % recording wavelength in [um]
  lambda_r=lambda_r*1e-3;      %nm to um

  % Sellmeier equation for PTR glass
  % index modulation of glass at recording wavelength 325 nm

  ng_w = 1.53054205492;
  %ng_w=sqrt(1+0.807152981395406*((lambda_w)^2)/(((lambda_w)^2)-
0.00551626201288283)+0.405762329340634*((lambda_w)^2)/(((lambda_w)^2)-
0.0184767208540142)+0.53804287785623*((lambda_w)^2)/(((lambda_w)^2)-
98.0038164610754));

  % index modulation of glass at reading wavelength (Bragg wavelength)
  ng_r=sqrt(1+0.807152981395406*((lambda_r)^2)/(((lambda_r)^2)-
0.00551626201288283)+0.405762329340634*((lambda_r)^2)/(((lambda_r)^2)-
0.0184767208540142)+0.53804287785623*((lambda_r)^2)/(((lambda_r)^2)-
98.0038164610754));

  % refractive index of prism
  n_prism = 1.4816; %  refractive index of prism (n FS @ 325 nm 1.4816)
  %n_prism = ng_w;    % with index matching (BK7 the same index as PTR glass)

  % Finding the grating period
  % Snell's law
  theta_g=asind((1/ng_r)*sind(theta_Inc));
  % using Bragg Condition
  per=(lambda_r)/(2*ng_r*cosd(theta_g-theta_tilt));
  %% The angle of interferance of writing beams
  % Interference angle in glass between wavevectors (writing angle in glass)
  theta_wg_L=asind(lambda_w/(2*ng_w*per))-theta_tilt;
  theta_wg_R=asind(lambda_w/(2*ng_w*per))+theta_tilt;

  theta_wg2_L=90-theta_wg_L;   % angles in the glass with respect to the normal to
the incident
  theta_wg2_R=90-theta_wg_R;

  % calculation of angles inside the prism
  % snell's law
  theta_wpl_L = asind(ng_w/n_prism*sind(theta_wg2_L));
  theta_wpl_R = asind(ng_w/n_prism*sind(theta_wg2_R));

  theta_wp2_L = theta_wpl_L - alpha;
  theta_wp2_R = theta_wpl_R - alpha;
```

```matlab
    % % snell's law between prism and air
    % finding the incident angle on prism
    theta_wi_L = asind(n_prism*sind(theta_wp2_L));
    theta_wi_R = -asind(n_prism*sind(theta_wp2_R));

    % if theta_wi_L>0 or theta_wi_R>0 the incident beam is...
    % ...at the right side of the prism's surface normal...

    % if theta_wi_L<0 or theta_wi_R<0 the incident beam is
    % ...at the left side of the prism's surface normal
    %%
    % finding the index modulation with the desired diffraction efficiency

    % Index modulation
    delta_n=1e6.*(atanh(sqrt(DE)).*lambda_r.*1e-6.*cosd(theta_Inc))./(pi.*t.*1e-3);

    % The angle of rotation of the stages should be half of the incident angle of
writing on the prisms

    theta_StgL=theta_wi_L/2;
    theta_StgR=theta_wi_R/2;


    Main_theta_stgL = theta_StgL + alpha/2;
    Main_theta_stgR = theta_StgR - alpha/2;

    theta_interference=0.5*abs(theta_wi_R+sign(theta_wi_L*theta_wi_R)*theta_wi_L);

    %% error
    % Dan's program error
    %err=sign(theta_wi_L)*theta_interference*0.00301+0.258125+0.007+1*0.0056-
1*0.174681-0.022309-0.011846+0.005216+1*0.027805-
1*0.032138+1*0.024351+1*0.008359+1*0.021712+1*0.009604-1*0.030322;
    % New measured error
    %err = -0.111-0.094;
    err = -0.111-0.047;
    %err = 0;

    %% output
    period = per;
    TwL = theta_wg_L;
    TwR = theta_wg_R;
    thetainprism_L = theta_wi_L;
    thetainprism_R = theta_wi_R;
    TStgL = theta_StgL;
    TStgR = theta_StgR;
    Rot_stgL = Main_theta_stgL + err;
    Rot_stgR = Main_theta_stgR - err;
    dn = delta_n;
    nw = ng_w;
    nr = ng_r;

    Out = table(per,thetainprism_L, thetainprism_R, Rot_stgL,Rot_stgR,delta_n)
End
```

APPENDIX B: MATLAB CODE OF COUPLED-WAVE-ANALYSIS

```matlab
%% Rigourous Coupled Wave Analysis
% Higher order modes
% Diffraction regimes of Bragg and Raman-Nath

clear all;
close all;
clc;
format short

%% 1. Initialization
%Constants:
% lambda = 1; % wavelegth is normalized to 1
% k0 = 2*pi/lambda;

% Given Data:
n0=1;
n1 = 1.5019;
%theta_i_deg0 =0;
%figure
tt=0;
t1=10;
st=0.05
t = -t1:st:t1;
NN = 1;
N3 = 2*NN + 1;
DD = zeros(size(t,2),N3);
RR = zeros(size(t,2),N3);

for theta_i_deg0=-t1:st:t1
tt=tt+1
t0 = find(t==0);
d = 2.2e-3;  % thickness [m]
lambda0 = 532e-9;  % wavelength in vacuum [m]
per = 28e-6;  % period of grating [m]
dn = 851e-6;     % index modulation
% Defined variables to be used in the analysis:
ratdlam = d/lambda0;
ratLlam = per/lambda0;
ratWL = 0.5;
n2 = n1 + dn;
ratdL = ratdlam / ratLlam;
rho = lambda0.^2./(per.^2*n1*dn);
if rho <= 1
    msg0 = ['Raman-Nath diffraction regime- {\rho} =',num2str(rho)];
elseif 1 <rho && rho <= 10
    msg0 = ['Intermediate diffraction regime- {\rho} =',num2str(rho)];
else rho > 10
    msg0 = ['Bragg diffraction regime - {\rho} =',num2str(rho)];
end
% Snell's Law: n0 * sin(theta_i_deg0) = n1 * sin (theta_i_deg);
theta_i_deg = asind(n0 .* sind(theta_i_deg0)./n1);
%theta_i_deg = 0;
theta_i = degtorad(theta_i_deg);
%NN = 10;
% Structure Loop
DET_orders = zeros(NN,1);
DER_orders = zeros(NN,1);
s=1;
zz=0;
for yy = -NN:NN
zz=zz+1
% msg1 = ['DE Reflected Orders for TE mode Structure-',num2str(s)];
% msg2 = ['DE Transmitted Orders for TE mode Structure-',num2str(s)];
% kx0 = k0*n1*sin(theta_i);
% kz0 = k0*n1*cos(theta_i);
```

```matlab
% Defined variables to be used in the analysis:
N1 = NN;
N2 = NN;
h = -2*N1:2*N2; % Epsilon harmonics limits
len = N1+N2+1; % Field harmonics limit
% Grating Periodic Permitivity
%Ep_h
Ep_h = ratWL*(n2^2-n1^2).*sin(pi.*h.*ratWL)./(pi.*h.*ratWL);
h0 = max(h)+1; %Ep_0 index
Ep_h(h0) = n1^2+ratWL*(n2^2-n1^2);
% E Matrix
E = zeros(N1,N2);
for i = 1:len
    for j = 1:len
        E(i,j) = Ep_h(h0+i-j);
    end
end
%E
m = -N1:N2;
m0 = find(m==0);
kxm = n1*sin(theta_i)-m/ratLlam;
Kx = diag(kxm);
% A matrix
A = E-Kx.^2;
[W, q2] = eig(A);
[W, q2] = sortem(W, q2);
q = zeros(1,length(A));
for i = 1:length(A)
q(i) = sqrt(q2(i,i));
end
% Ordering Eigenvalues
q = real(q)-imag(q).*1i; % After taking squareroot, doing this to keep the
eigenvalues in order
%q = fliplr(q);
%W flip
%W = fliplr(W);
%V matrix
V = W*diag(q);
% Normal Components
k1z = sqrt(n1^2-kxm.^2);
k1z = real(k1z)-imag(k1z).*1i;
K1Z = diag(k1z);
k2z = sqrt(n2^2-kxm.^2);
k2z = real(k2z)-imag(k2z).*1i;
K2Z = diag(k2z);
% X matrix
Xd = exp(-1i.*q.*2*pi.*ratdlam);
Xd = diag(Xd);
a = K1Z*W+V;
b = (K1Z*W-V)*Xd;
c = (K2Z*W-V)*Xd;
d = K2Z*W+V;
M1 = [a,b;c,d];
syms kk;
kk = sym(m);
Kdelta = double(kroneckerDelta(kk))';
Zero = zeros(size(K1Z));
B1 = [2*K1Z; Zero];
%whos B1 Kdelta
B = B1*Kdelta;
C = M1\B;
c_forw = C(1:length(C)/2);
c_backw = C(length(c_forw)+1:end);
%whos c_forw c_backw
R = W*(c_forw + Xd*c_backw)-Kdelta;
T = W*(Xd*c_forw + c_backw);
```

```matlab
DER = abs(R).^2.*(real(k1z)'/k1z(m0))*100; % Diffraction efficiency (%) for
Reflected Field
DET = abs(T).^2.*(real(k2z)'/k1z(m0))*100; % Diffraction efficiency (%) for
Transmitted Field
sumDERT = sum(DER)+sum(DET);% Total Diffraction Efficiency (%)
%Total(NN-2,:) = [len;sum(DER);sum(DET);sumDERT];
DET_orders(zz) = DET(m0+yy);
DER_orders(zz) = DER(m0+yy);
%DET_II(zz,dlam) = DET(m0+yy);
end % order loop
%end
DD(tt,:) = DET_orders;
RR(tt,:) = DER_orders;
% plot(m',DET_orders,'*', 'linewidth',4)
% xlabel('orders', 'fontsize', 17);
% ylabel('Diff. Efficiency (%)', 'fontsize', 17);
% set(gca,'FontSize',16);
% title(msg0)
% grid minor
% hold on
end
figure;
for ang = 1:N3
dd = DD(:,ang);
plot(t,dd,'linewidth', 2); grid minor;
title('Angular dependence')
xlabel('Angle of rotation (deg)','fontsize', 17);
ylabel('DE (%)', 'fontsize', 17);
set(gca,'FontSize',16);
legendInfo{ang} = ['m = ' num2str(ang-m0)];
hold on
legend(legendInfo)
end
figure;
for ang = 1:N3
rr = RR(:,ang);
plot(t,rr,'linewidth', 2); grid minor;
title('Angular dependence')
xlabel('Angle of rotation (deg)','fontsize', 17);
ylabel('DE (%)', 'fontsize', 17);
set(gca,'FontSize',16);
legendInfo{ang} = ['m = ' num2str(ang-m0)];
hold on
legend(legendInfo)
end
```

REFERENCES

1. Kannatey-Asibu Jr E. *Principles of laser materials processing.* Vol 4: John Wiley & Sons; 2009.

2. Lawrence JR, Waugh D. *Laser surface engineering: Processes and applications.* Elsevier; 2014.

3. Lawrence JR. *Advances in laser materials processing: Technology, research and applications.* Woodhead Publishing; 2017.

4. Grier DG. A revolution in optical manipulation. *nature.* 2003;424(6950):810-816.

5. Gibson G, Courtial J, Padgett MJ, et al. Free-space information transfer using light beams carrying orbital angular momentum. *Optics express.* 2004;12(22):5448-5456.

6. Wang J, Yang J-Y, Fazal IM, et al. Terabit free-space data transmission employing orbital angular momentum multiplexing. *Nature photonics.* 2012;6(7):488-496.

7. Willner AE, Huang H, Yan Y, et al. Optical communications using orbital angular momentum beams. *Advances in Optics and Photonics.* 2015;7(1):66-106.

8. Isenhower L, Williams W, Dally A, Saffman M. Atom trapping in an interferometrically generated bottle beam trap. *Optics letters.* 2009;34(8):1159-1161.

9. Planchon TA, Gao L, Milkie DE, et al. Rapid three-dimensional isotropic imaging of living cells using bessel beam plane illumination. *Nature methods.* 2011;8(5):417-423.

10. Parigi V, D'Ambrosio V, Arnold C, Marrucci L, Sciarrino F, Laurat J. Storage and retrieval of vector beams of light in a multiple-degree-of-freedom quantum memory. *Nature communications.* 2015;6(1):1-7.

11. Leach J, Jack B, Romero J, et al. Quantum correlations in optical angle–orbital angular momentum variables. *Science.* 2010;329(5992):662-665.

12. Lindlein N, Leuchs G, Ramachandran S. Achieving gaussian outputs from large-mode-area higher-order-mode fibers. *Applied optics.* 2007;46(22):5147-5157.

13. Gregg P, Mirhosseini M, Rubano A, et al. Q-plates as higher order polarization controllers for orbital angular momentum modes of fiber. *Optics letters.* 2015;40(8):1729-1732.

14. Gerber M, Graf T, Kudryashov A. Generation of custom modes in a nd: Yag laser with a semipassive bimorph adaptive mirror. *Applied Physics B.* 2006;83(1):43-50.

15. Lubeigt W, Valentine G, Girkin J, Bente E, Burns D. Active transverse mode control and optimisation of an all-solid-state laser using an intracavity adaptive-optic mirror. *Optics Express.* 2002;10(13):550-555.

16. Ngcobo S, Litvin I, Burger L, Forbes A. A digital laser for on-demand laser modes. *Nature communications.* 2013;4(1):1-6.

17. Forbes A. *Laser beam propagation: Generation and propagation of customized light.* CRC Press; 2014.

18. SeGall M, Rotar V, Lumeau J, Mokhov S, Zeldovich B, Glebov LB. Binary volume phase masks in photo-thermo-refractive glass. *Optics letters.* 2012;37(7):1190-1192.

19. Glebov LB. Volume holographic elements in a photo-thermo-refractive glass. *Journal of Holography and Speckle.* 2009;5(1):77-84.

20. SeGall M, Divliansky I, Jollivet C, Schülzgen A, Glebov LB. Holographically encoded volume phase masks. *Optical Engineering.* 2015;54(7):076104.

21. Kogelnik H. Coupled wave theory for thick hologram gratings. *Landmark papers on photorefractive nonlinear optics*: World Scientific; 1995:133-171.

22. Divliansky I, Hale ER, SeGall M, Glebov LB. Achromatic complex holograms for laser mode conversion. *Optics Express.* 2019;27(1):225-239.

23. Glebov L, Smirnov V, Tabirian N, Zeldovich B. *Implementation of 3d angular selective achromatic diffraction optical grating device.* UNIVERSITY OF CENTRAL FLORIDA ORLANDO SCHOOL OF OPTICS/CREOL;2004.

24. Mhibik O, Divliansky I, Segall M, Glebov L. Achromatic holographic phase mask for broadband lasers beam conversion (conference presentation). Paper presented at: Laser Resonators, Microresonators, and Beam Control XXII2020.

25. Dickey FM, Lizotte TE. *Laser beam shaping applications.* Vol 1: CRC Press; 2017.

26. Dickey FM. *Laser beam shaping: Theory and techniques.* CRC press; 2018.

27. Forbes A. Structured light from lasers. *Laser & Photonics Reviews.* 2019;13(11):1900140.

28. Bozinovic N, Yue Y, Ren Y, et al. Terabit-scale orbital angular momentum mode division multiplexing in fibers. *science.* 2013;340(6140):1545-1548.

29. Allen L, Beijersbergen MW, Spreeuw R, Woerdman J. Orbital angular momentum of light and the transformation of laguerre-gaussian laser modes. *Physical review A.* 1992;45(11):8185.

30. Yao AM, Padgett MJ. Orbital angular momentum: Origins, behavior and applications. *Advances in Optics and Photonics.* 2011;3(2):161-204.

31. Hariharan P. *Basics of holography.* Cambridge university press; 2002.

32. Bragg WH, Bragg WL. *X rays and crystal structure.* G. Bell; 1924.

33. Ciapurin IV, Glebov LB, Smirnov VI. Modeling of gaussian beam diffraction on volume bragg gratings in ptr glass. Paper presented at: Practical Holography XIX: Materials and Applications2005.

34. Ciapurin IV, Glebov LB, Smirnov VI. Spectral combining of high-power fiber laser beams using bragg grating in ptr glass. Paper presented at: Fiber Lasers: Technology, Systems, and Applications2004.

35. Lin L. Method of characterizing hologram-recording materials. *JOSA.* 1971;61(2):203-208.

36. Collier R. *Optical holography.* Elsevier; 2013.

37. Efimov OM, Glebov LB, Smirnov VI. Diffractive optical elements in photosensitive inorganic glasses. Paper presented at: Inorganic Optical Materials III2001.

38. Efimov O, Glebov L, Smirnov V. High-frequency bragg gratings in a photothermorefractive glass. *Optics Letters.* 2000;25(23):1693-1695.

39. Glebov LB. Kinetics modeling in photosensitive glass. *Optical Materials.* 2004;25(4):413-418.

40. Glebov L. Fluorinated silicate glass for conventional and holographic optical elements. Paper presented at: Window and Dome Technologies and Materials X2007.

41. Curtis JE, Koss BA, Grier DG. Dynamic holographic optical tweezers. *Optics communications.* 2002;207(1-6):169-175.

42. Lesem L, Hirsch P, Jordan J. The kinoform: A new wavefront reconstruction device. *IBM Journal of Research and Development.* 1969;13(2):150-155.

43. Hirsch PM, Jordan Jr JA, Lesem LB. Method of making an object dependent diffuser. Google Patents; 1971.

44. Gerchberg RW. A practical algorithm for the determination of phase from image and diffraction plane pictures. *Optik.* 1972;35:237-246.

45. Qiao Z, Kong L, Xie G, et al. Ultraclean femtosecond vortices from a tunable high-order transverse-mode femtosecond laser. *Optics Letters.* 2017;42(13):2547-2550.

46. Xie C, Jukna V, Milián C, et al. Tubular filamentation for laser material processing. *Scientific reports.* 2015;5(1):1-8.

47. Nivas JJ, He S, Rubano A, et al. Direct femtosecond laser surface structuring with optical vortex beams generated by a q-plate. *Scientific reports.* 2015;5(1):1-12.

48. Sola I, Collados V, Plaja L, et al. High power vortex generation with volume phase holograms and non-linear experiments in gases. *Applied Physics B.* 2008;91(1):115-118.

49. Stutzki F, Otto H-J, Jansen F, et al. High-speed modal decomposition of mode instabilities in high-power fiber lasers. *Optics Letters.* 2011;36(23):4572-4574.

50. Flamm D, Naidoo D, Schulze C, Forbes A, Duparré M. Mode analysis with a spatial light modulator as a correlation filter. *Optics letters.* 2012;37(13):2478-2480.

51. Divliansky I. Volume bragg gratings: Fundamentals and applications in laser beam combining and beam phase transformations. *Holographic Materials and Optical Systems.* 2017:51.

52. Ott D, Divliansky I, Anderson B, Venus G, Glebov L. Scaling the spectral beam combining channels in a multiplexed volume bragg grating. *Optics express.* 2013;21(24):29620-29627.

53. Mach LH, Mohammadian N, Mhibik O, Glebov L, Divliansky I. Intracavity spatial mode conversion by mean of holographic phase masks. Paper presented at: Solid State Lasers XXX: Technology and Devices2021.

54. Jundt DH. Temperature-dependent sellmeier equation for the index of refraction, n e, in congruent lithium niobate. *Optics letters.* 1997;22(20):1553-1555.

55. Lee Y-H, Zhan T, Wu S-T. Prospects and challenges in augmented reality displays. *Virtual Real Intell Hardw.* 2019;1(1):10-20.

56. Martinez MA, Saeedi E, Amirparviz B. Head-mounted display including integrated projector. Google Patents; 2015.

57. Wang J, Liang Y, Xu M. Design of a see-through head-mounted display with a freeform surface. *Journal of the Optical Society of Korea.* 2015;19(6):614-618.

58. Pulli K. 11-2: Invited paper: Meta 2: Immersive optical-see-through augmented reality. Paper presented at: SID Symposium Digest of Technical Papers2017.

59. Takahashi K. Head or face mounted image display apparatus. Google Patents; 1997.

60. Cheng D-w, Wang Y-t, Chang J, Liu Y, Xu K. Design of a lightweight and wide field-of-view hmd system with free-form-surface prism. *Infrared and Laser Engineering.* 2007;36(3):309.

61. Gu L, Cheng D, Wang Q, Hou Q, Wang Y. Design of a two-dimensional stray-light-free geometrical waveguide head-up display. *Applied Optics.* 2018;57(31):9246-9256.

62. Cheng D, Wang Y, Xu C, Song W, Jin G. Design of an ultra-thin near-eye display with geometrical waveguide and freeform optics. *Optics express.* 2014;22(17):20705-20719.

63. Brooker G. *Modern classical optics.* Vol 8: Oxford University Press; 2003.

64. Jang C, Bang K, Li G, Lee B. Holographic near-eye display with expanded eye-box. *ACM Transactions on Graphics (TOG).* 2018;37(6):1-14.

65. Häussler R, Reichelt S, Leister N, Zschau E, Missbach R, Schwerdtner A. Large real-time holographic displays: From prototypes to a consumer product. Paper presented at: Stereoscopic Displays and Applications XX2009.

66. Chen R, Maimone A, Fuchs H, Raskar R, Wetzstein G. Wide field of view compressive light field display using a multilayer architecture and tracked viewers. *Journal of the Society for Information Display.* 2014;22(10):525-534.

67. Migozzi J-B. Optical device enabling the introduction of a collimated image in an observer's field of vision. Google Patents; 1991.

68. Maimone A. Projector-combiner display with beam replication. Google Patents; 2020.

69. Kress BC. Optical waveguide combiners for headsets: Features and limitations. Paper presented at: Digital Optical Technologies 20192019.

70. Wang C-J. Near-to-eye display having adaptive optics. Google Patents; 2015.

71. Bragg WH, Bragg WL. The reflection of x-rays by crystals. *Proceedings of the Royal Society of London Series A, Containing Papers of a Mathematical and Physical Character.* 1913;88(605):428-438.

72. Nath NN. The diffraction of light by supersonic waves in solids. Paper presented at: Mathematical Proceedings of the Cambridge Philosophical Society1938.

73. Raman C, Nathe NN. The diffraction of light by high frequency sound waves: Part i. Paper presented at: Proceedings of the Indian Academy of Sciences-Section A1935.

74. Klein W, Cook B, Mayer W. Light diffraction by ultrasonic gratings. *Acta Acustica united with Acustica.* 1965;15(2):67-74.

75. Magnusson R, Gaylord T. Analysis of multiwave diffraction of thick gratings. *JOSA.* 1977;67(9):1165-1170.

76. Moharam M, Young L. Criterion for bragg and raman-nath diffraction regimes. *Applied optics.* 1978;17(11):1757-1759.

77. Baird W, Moharam M, Gaylord T. Diffraction characteristics of planar absorption gratings. *Applied Physics B.* 1983;32(1):15-20.

78. Gaylord TK, Moharam M. Thin and thick gratings: Terminology clarification. *Applied optics.* 1981;20(19):3271-3273.

79. Gaylord T, Moharam M. Planar dielectric grating diffraction theories. *Applied Physics B.* 1982;28(1):1-14.

80. Divliansky I, Ott D, Anderson B, et al. Multiplexed volume bragg gratings for spectral beam combining of high power fiber lasers. Paper presented at: Fiber Lasers IX: Technology, Systems, and Applications2012.